

## The “Triple Point” on 24 May 2002 during IHOP. Part II: Ground-Radar and In Situ Boundary Layer Analysis of Cumulus Development and Convection Initiation

CONRAD L. ZIEGLER

*NOAA/National Severe Storms Laboratory, Norman, Oklahoma*

ERIK N. RASMUSSEN AND MICHAEL S. BUBAN

*Cooperative Institute for Mesoscale Meteorological Studies, University of Oklahoma, Norman, Oklahoma*

YVETTE P. RICHARDSON

*Department of Meteorology, The Pennsylvania State University, University Park, Pennsylvania*

L. JAY MILLER

*National Center for Atmospheric Research, Boulder, Colorado*

ROBERT M. RABIN

*NOAA/National Severe Storms Laboratory, Norman, Oklahoma*

(Manuscript received 23 January 2006, in final form 28 August 2006)

### ABSTRACT

Cumulus formation and convection initiation are examined near a cold front–dryline “triple point” intersection on 24 May 2002 during the International H<sub>2</sub>O Project (IHOP). A new Lagrangian objective analysis technique assimilates in situ measurements using time-dependent Doppler-derived 3D wind fields, providing output 3D fields of water vapor mixing ratio, virtual potential temperature, and lifted condensation level (LCL) and water-saturated (i.e., cloud) volumes on a subdomain of the radar analysis grid. The radar and Lagrangian analyses reveal the presence of along-wind (i.e., longitudinal) and cross-wind (i.e., transverse) roll circulations in the boundary layer (BL). A remarkable finding of the evolving radar analyses is the apparent persistence of both transverse rolls and individual updraft, vertical vorticity, and reflectivity cores for periods of up to 30 min or more while moving approximately with the local BL wind. Satellite cloud images and single-camera ground photogrammetry imply that clouds tend to develop either over or on the downwind edge of BL updrafts, with a tendency for clouds to elongate and dissipate in the downwind direction relative to cloud layer winds due to weakening updrafts and mixing with drier overlying air. The Lagrangian and radar wind analyses support a parcel continuity principle for cumulus formation, which requires that rising moist air parcels achieve their LCL before moving laterally out of the updraft. Cumuli form within penetrative updrafts in the elevated residual layer (ERL) overlying the moist BL east of the triple point, but remain capped by a convection inhibition (CIN)-bearing layer above the ERL. Dropsonde data suggest the existence of a convergence line about 80 km east of the triple point where deep lifting of BL moisture and locally reduced CIN together support convection initiation.

### 1. Introduction

The weather research community, through the U. S. Weather Research Program (USWRP), has established

---

*Corresponding author address:* Dr. Conrad L. Ziegler, Forecast Research and Development Division, National Severe Storms Laboratory, 120 David L. Boren Blvd., Norman, OK 73072.  
E-mail: conrad.ziegler@noaa.gov

the objective to improve the specificity, accuracy, and reliability of weather forecasts of disruptive, high impact weather, particularly of the initiation and evolution of severe storms and heavy convective precipitation (Fritsch et al. 1998). During May–June 2002, the International H<sub>2</sub>O Project (IHOP) observed the boundary layer (BL) on the U.S. southern Great Plains with a dense array of mobile observing systems to de-

DOI: 10.1175/MWR3411.1

© 2007 American Meteorological Society

duce the processes governing convection initiation<sup>1</sup> (CI) near surface-based boundaries<sup>2</sup> (Weckwerth et al. 2004). In response to the USWRP objective to improve storm forecasts, IHOP directly addressed several key aspects of the USWRP's warm-season quantitative precipitation forecasting (QPF) theme. A focus of IHOP was to learn how the coevolving fields of BL airflow, temperature, and water vapor control the initiation or suppression of deep, moist convection.

A robust conceptual understanding of the CI process would help improve forecasts of convective weather phenomena, including both severe storms (Johns and Doswell 1992) and flash flooding caused by storms (Doswell et al. 1996). Brooks et al. (1992) argue that improved forecasts of convective weather phenomena require improved CI forecasts, and improved knowledge of the CI process provides a foundation for improved forecasts. The impact of CI on the warm-season QPF process bears analogy to a decision point in a semichaotic system (Stensrud and Bao 1992) wherein persistent, potentially severe or flash flood-producing convection is set in motion depending on the CI probability. Events in which the CI probability may be low or difficult to assess due to lack of local observations are particularly challenging, especially if such a CI event occurs outside the region possessing favorable severe weather or flash flood potential (e.g., Rockwood and Maddox 1988). The present paper reports an analysis of the processes leading to cumulus formation and the initiation of deep convective clouds on 24 May using IHOP's mobile observations.

Combining airflow, temperature, and moisture measurements with photographic and radar documentation of cloud and storm development in common analysis volumes, several pre-IHOP studies have demonstrated a direct connection between lifting near and along surface boundaries and either cumulus formation or CI. For example, Wilson et al. (1992) showed that deep updrafts along the Denver convergence line initiated cumulus clouds and storms. Using radar measurements of storm growth, Wilson and Schreiber (1986) determined that CI frequency and location was controlled by evolving surface-based convergence lines, storm out-

flows, and their complex interactions. Atkins et al. (1995) showed that cumuli developed at intersection points of the Florida sea breeze front and horizontal convective rolls (HCRs). Shapiro et al. (1985), Koch and Clark (1999), and Miller et al. (1996) analyzed strong cold fronts, which formed cumulus cloud lines along their leading edges. Ziegler and Rasmussen (1998, hereafter ZR98) showed that cumuli develop along or close to the dryline, while Atkins et al. (1998) proposed that cumuli develop at the intersection points of the dryline with HCRs. In each of the above cases, updrafts at cloud locations were adequately deep for air parcels to achieve their lifting condensation level (LCL) and were inferred to form cumulus clouds. While not analyzing the 3D airflow from BL radar measurements as in several of the former cases, the cold frontal cases of Shapiro et al. (1985) and Koch and Clark (1999), and the dryline cases of Ziegler et al. (1997) and Hane et al. (1997, 2002) inferred vertical motions adequately deep for moist parcels to achieve their level of free convection (LFC) in those observed CI events. A common limitation of CI studies is the inherent complexity of actual BL air trajectories combined with a paucity of direct measurements of the LCL and LFC on those trajectories, making it difficult to identify the subset of BL trajectories with the highest CI potential.

Connections between cumulus cloud formation and radar-indicated CI locations and BL updrafts have been investigated in greater detail with IHOP observations (Weckwerth and Parsons 2006). Arnott et al. (2006) and Markowski et al. (2006) determined that photogrammetrically mapped cumulus cloud bases were located in or at the edges of multiple Doppler radar-derived BL updrafts both along and ahead of the slow-moving 10 June cold front and 12 June outflow boundary, respectively. Backward radar airflow trajectories calculated from the mapped cloud bases in the 12 June case verified that clouds were fed by moist air rising from lower in the BL. Karan and Knupp (2006, hereafter K06), documented a correspondence between profiler-measured BL updrafts and ceilometer-indicated cloud bases from the mobile integrated profiling system (MIPS) observations of the 24 May BL and cold frontal passage. Weiss et al. (2006) employed a vertically pointing camera and a scanning W-band radar to document deep BL updraft plumes located beneath high-based cumulus and cumulus fractus clouds west of the 22 May dryline. Murphey et al. (2006) documented the development of a deep secondary circulation and collocation of strong, deep BL updraft cores at the bases of developing deep, moist convective echoes just east of the dryline in the 19 June case.

<sup>1</sup> The term CI is defined herein as the process that initiates the formation of a cumulonimbus, a deep, moist convective cloud with an anvil, an active precipitation growth process, and intracloud/cloud-to-ground lightning.

<sup>2</sup> The term boundary is defined as a transition zone between boundary layers of dissimilar temperature and humidity, typically in concert with and frequently delineated by horizontal convergence and shear. Two categories are classical synoptic airmass boundaries (e.g., drylines and cold fronts) and nonclassical boundaries forced by contrasting local surface heat fluxes.

Simple 1D parcel theory neglects the effects of vertical shear, the length and velocity scales of the updraft, and variability of the LCL and LFC while requiring only the joint occurrence of low-level convergence and updrafts in a moist convectively unstable atmosphere as ingredients to anticipate cloud development and CI (e.g., Banacos and Schultz 2005). In preparation for IHOP, two of the coauthors (C. Ziegler and E. Rasmussen) proposed an alternative testable hypothesis that is predicated on the 3D structure of BL airflow and requires that rising air parcels must achieve their LCL (or alternatively the LFC) before moving laterally out of the updraft for cumulus formation or CI to occur (ZR98). The latter conceptual model, which may be termed the parcel continuity principle, effectively restricts the length and velocity scales of the 3D airflow to satisfy an inequality constraint between the time scales of horizontal and vertical advection (as described in detail below) while placing no restrictions on the variability of parcel LCL or LFC in the BL. Indeed, since clouds entrain mixtures of air from varying BL levels, both operational experience (Craven et al. 2002) and mesoscale simulations of the dryline environment (Ziegler et al. 1997) indicate that layer-average BL parcel parameters are generally more representative of convective cloud properties than surface parcel parameters. Parcel theory approximately holds in special circumstances such as intense thunderstorm updrafts (Davies-Jones 1974; Bluestein et al. 1988) or deep, erect dryline updrafts that generate moist absolutely unstable layers (Ziegler et al. 1997). On the other hand, the parcel continuity principle represents a continuum of states proceeding from quiescent prestorm BL conditions through cumulus formation to CI, and also reduces to parcel theory in the latter special cases where vertical advection dominates.

Using IHOP observations, the present study quantifies the local airflow, moisture, and temperature state conditions that together either support or inhibit cumulus formation and CI in accordance with the parcel continuity principle. Although forecasters do not yet have access to all types of high-resolution data utilized in this study, the present research nevertheless provides the basis for new conceptual models and methods for applying available measurements that human forecasts may utilize. The present research further illustrates what forecast improvements may be possible given the right mix and resolution of mesoscale observations.

## 2. Observations and data analysis methods

The present study combines ground-based mobile radar and in situ observations from airborne and ground-

based mobile platforms to analyze the BL in the vicinity of the “triple point” intersection of a dryline and cold front on 24 May 2002 during the IHOP experiment. The current results will be placed in the context of an analysis of the 24 May dryline and cold front using Naval Research Laboratory (NRL) P-3 airborne radar, Learjet dropsonde, and National Aeronautics and Space Administration (NASA) DC-8 vertically pointing differential absorption lidar (DIAL) observations (Wakimoto et al. 2006, hereafter W06) and a fine-resolution study of the 24 May cold front with the Wyoming Cloud Radar (WCR; Geerts et al. 2006, hereafter G06).

On 24 May, the National Severe Storms Laboratory (NSSL) operated the Shared Mobile Atmospheric Research and Teaching (SMART) 5-cm Doppler Radar (SR1; Biggerstaff et al. 2005), seven mobile mesonets (Straka et al. 1996; Ziegler et al. 2004), a mobile Cross-Chain Loran Atmospheric Sounding System (CLASS) vehicle (Rust et al. 1990), and a field coordination (FC) vehicle (Ziegler et al. 2004) from their base in Norman, Oklahoma. Deployed from their base in Liberal, Kansas, the “Doppler-on-Wheels” DOW2, DOW3, and XPOL 3-cm Doppler radars (Wurman 2001; Wurman et al. 1997), two National Center for Atmospheric Research (NCAR) mobile GPS/Loran Atmospheric Sounding System (GLASS) vehicles, and the University of Alabama at Huntsville MIPS (K06) joined with the NSSL facilities in the eastern Texas panhandle around 1800 UTC. The ground-based platforms concentrated measurements within an intensive observing region (IOR) about 50 km on a side and centered in the triple point vicinity. The NRL P-3 and Wyoming King Air (KA) research aircraft deployed from Will Rogers World Airport in Oklahoma City, Oklahoma, providing in situ BL data in the IOR beginning during the early afternoon (W06; G06). Ground-based radar data were collected starting from synchronized base sweeps of up to four radars at either 1.5-min intervals (DOWs) or 3-min intervals (SR1) between 1815 and 2015 UTC.

### a. Ground-based mobile radar analysis

The multiple ground-based radar analysis is briefly summarized in the present section, with details described by Ziegler et al. (2007). The ground-based mobile radar data have been extensively edited using NCAR’s SOLO software program (Oye et al. 1995). After time-to-space adjustment of data locations at a velocity of  $225^\circ$  at  $4.6 \text{ m s}^{-1}$  to correct for the movement of updraft and reflectivity cores and misocyclones, Barnes weighting (Barnes 1973; Koch et al. 1983) is used to interpolate radial velocity and reflectivity data to a 3D Cartesian analysis grid with NCAR’s

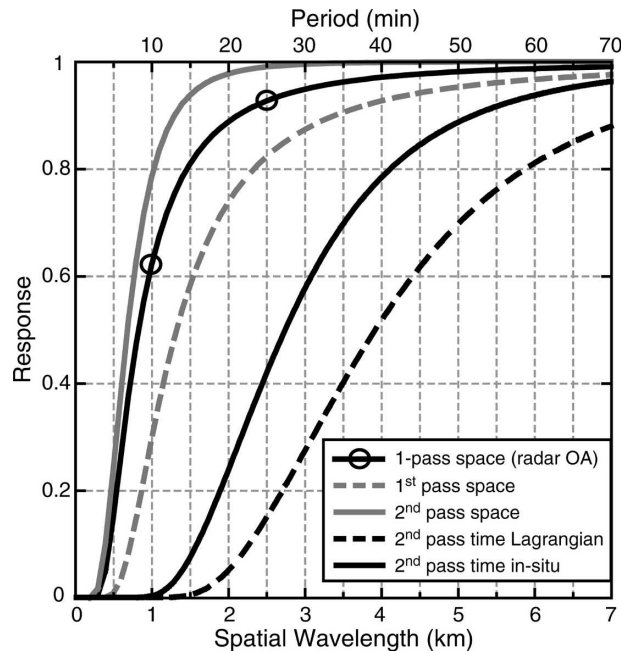


FIG. 1. Spectral responses of the Barnes spatial and temporal objective analysis weighting functions for the 24 May 2002 case study.

REORDER software (Oye et al. 1995). The Barnes weighting function has the form  $w = \exp(-r^2/\kappa)$ , where  $r$  is the distance between a grid point and a datum. The low-pass-filter response of the Barnes analysis (Fig. 1) is controlled by prescribing its smoothing parameter  $\kappa$  (Table 1). The spatial dimensions of the Cartesian radar analysis domain are 50 km  $\times$  50 km horizontally and 2.5 km vertically, while the corresponding horizontal and vertical radar analysis grid spacings are 0.5 and 0.25 km, respectively.

Gridded single Doppler fields are combined to produce fields of composite reflectivity and synthesized 3D airflow employing upward integration of mass continuity from  $w = 0$  at ground and the overdetermined two-radar analysis option of NCAR's Custom Editing and Display of Reduced Information in Cartesian Space (CEDRIC) software (Mohr et al. 1986). The interpolated reflectivities from DOW radars are linearly scaled

for optimal consistency with the calibrated SR1 reflectivities. A gridded reflectivity analysis is composited by assigning each gridpoint the first nonmissing objectively analyzed single radar value from either DOW2, DOW3, XPOL, or SR1 (i.e., in that order of precedence). Multi-Doppler radar analyses are obtained at 3-min intervals during the period of 1815–2015 UTC (Table 2). The wind synthesis employs an optimal combination of radars that minimizes sampling errors of the shallow cold front (Ziegler et al. 2007). Judging from the temporal continuity of individual moving cores of reflectivity, vertical velocity, and vertical vorticity in results to be presented, a 3-min analysis interval appears sufficient to resolve the evolution of the meso- $\gamma$  scale ( $\sim$ 1–10 km wavelength) boundary layer circulations of interest for this study.

### b. Lagrangian analysis of thermal variables

The essential aspects of the Lagrangian analysis scheme are summarized in this section, with details described by Ziegler et al. (2007). In brief, a Lagrangian principle is employed to propagate sparse in situ observations along up- and downstream air trajectories assuming conservation following the motion, providing an enhanced dataset for 3D objective analysis. The Lagrangian analysis proceeds via a multistep approach, including the preconditioning of wind and in situ data, the generation of air trajectories from in situ data and grid-column soundings (described below), and a 3D, two-pass Barnes objective analysis of all Lagrangian trajectory data. The Barnes weighting function takes the form  $w = \exp[-(r^2/\kappa_s) - (t_i^2/\tau_i) - (t_L^2/\tau_L)]$ , where  $t_i$  is the time difference between an observation time and the nominal map time and  $t_L$  is elapsed time along a trajectory. The spatial and temporal low-pass-filter responses (Fig. 1) are controlled by setting the Barnes smoothing parameters  $\kappa$  and  $\tau$  (see Table 1).

In situ observations from mobile mesonets, mobile soundings, and aircraft are augmented in mesoscale boundary layer updrafts by pseudo-soundings derived by adjusting a reference sounding profile according to the local surface Lagrangian analysis value derived

TABLE 1. Barnes filter parameters and response values at selected wavelength (km) or period (min) for the temporal and spatial Barnes weighting in the radar and Lagrangian objective analyses in the 24 May case study. The filter parameter (Barnes 1973; Koch et al. 1983) is denoted by either  $\kappa$  or  $\tau$  for spatial and temporal weighting, respectively. The convergence parameter  $\gamma = 0.3$  for the two-pass Lagrangian objective analysis. The corresponding response functions are displayed in Fig. 1.

Objective analysis type	Barnes filtering parameter	Wavelength (km)/period (min) for 5% response	Wavelength (km)/period (min) for 80% response
Spatial (radar analysis)	$\kappa = 0.0486$	0.4 km (one pass)	1.5 km (one pass)
Spatial (Lagrangian analysis)	$\kappa_s = 0.124$	0.35 km (2d pass)	1 km (2d pass)
Temporal (initial condition)	$\tau_i = 714\ 113$	14 min (2d pass)	41 min (2d pass)
Temporal (Lagrangian point)	$\tau_L = 1\ 457\ 374$	20 min (2d pass)	58 min (2d pass)

TABLE 2. Multi-Doppler radar analysis history on 24 May 2002. Volume scan analyses (indicated by x) from DOW2, DOW3, and XPOL were spaced at a 1.5-min interval, SR1 volume scans were obtained every 3 min, and radar analyses were spaced at a 3-min interval. The rightmost two columns list the numerical sequence of radars available for analysis in the given time interval. The primary analysis was applied ahead of the cold front, while the secondary analysis was applied behind the cold front if a total of two or more radars were available at a given analysis time. The cold frontal position was defined by a best-fit line at each analysis time. No secondary analysis was employed prior to the entry of the cold front into the radar coverage at around 1854 UTC.

Time interval (UTC)	SR1 (1)	DOW2 (2)	DOW3 (3)	XPOL (4)	Total radars	Primary analysis	Secondary analysis
1815–1842	x	x			2	1, 2	None
1845–1851	x	x		x	3	1, 2, 4	None
1854	x			x	2	1, 4	None
1857–1921	x	x		x	3	1, 2, 4	2, 4
1924–2015	x	x	x	x	4	1, 2, 3, 4	2, 3, 4

from the dense mobile mesonet surface analysis (Ziegler et al. 2007). In the prefrontal BL case (i.e., on either side of the dryline), the local grid-column sounding is obtained by averaging percentages of the moist and dry side reference soundings along a mixing line with a mass fraction based on the local mixing ratio value of the surface analysis. In the postfrontal BL case, the reference sounding adjustment increases linearly from zero at the BL top to the difference between the surface reference sounding and surface analysis values. Three unique, air-mass-specific reference soundings are employed to globally represent observed soundings in

the respective air masses (i.e., predryline, between front and dryline, and postfrontal). Lagrangian variables include water vapor mixing ratio, potential temperature, and virtual potential temperature.

After decimating (i.e., sampling at a subinterval of) the input in situ data to restrict the analysis to resolvable scales, the analysis propagates in situ and gridpoint data along forward and backward 4D trajectories employing a quadratic Runge–Kutta predictor–corrector time integration scheme with trilinear spatial and linear time interpolation between neighboring input multi-Doppler analyses. The Lagrangian data are decimated

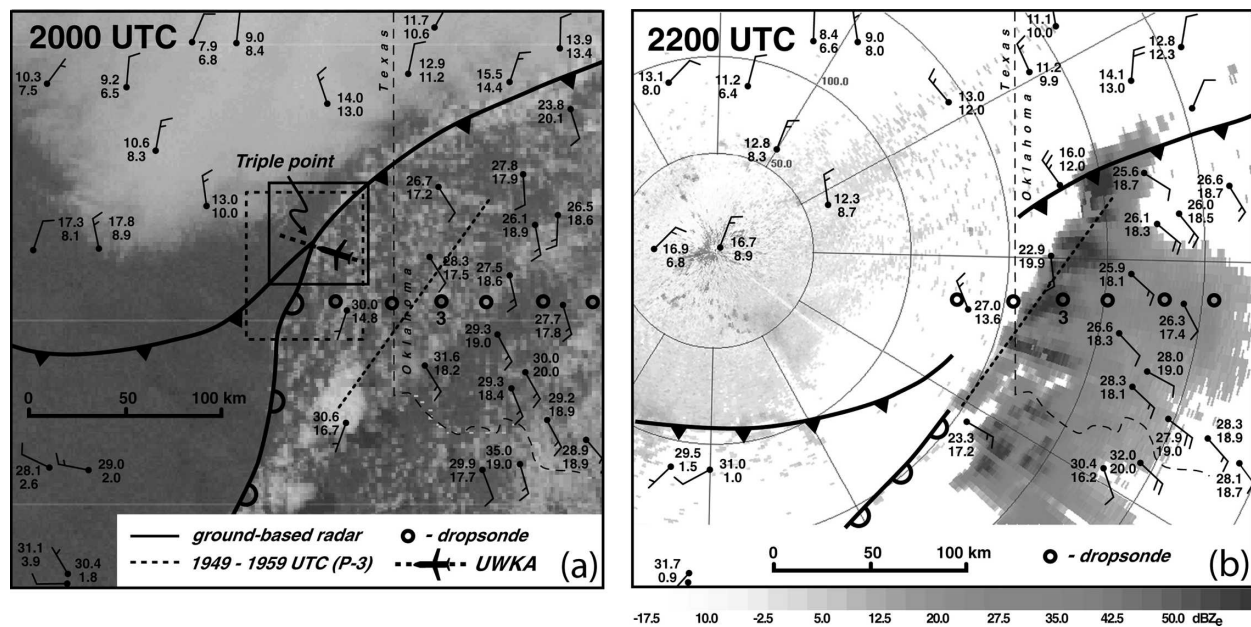


FIG. 2. Surface observations and dropsonde locations superimposed on (a) the 2000 UTC visible satellite image and (b) the 2200 UTC Weather Surveillance Radar-1988 Doppler (WSR-88D) base radar scan on 24 May 2002 (adapted from Fig. 2 of Wakimoto et al. 2006). The black solid box denotes the 50 km × 50 km radar analysis domain used in the present study, while the dashed rectangle locates the airborne pseudodoppler analysis domain of Wakimoto et al. (2006). The thick dashed line is the location of a stepped traverse performed by the University of Wyoming King Air (Geerts et al. 2006), while dropsonde locations during the period 2031–2046 UTC are indicated by open circles (e.g., drop 3 labeled for discussion in text). Station models for surface observations include wind (full barb = 5 m s<sup>-1</sup>, half barb = 2.5 m s<sup>-1</sup>) with temperature (°C) over dewpoint temperature (°C). The dotted line locates the axis of the initial deep convection in western Oklahoma.

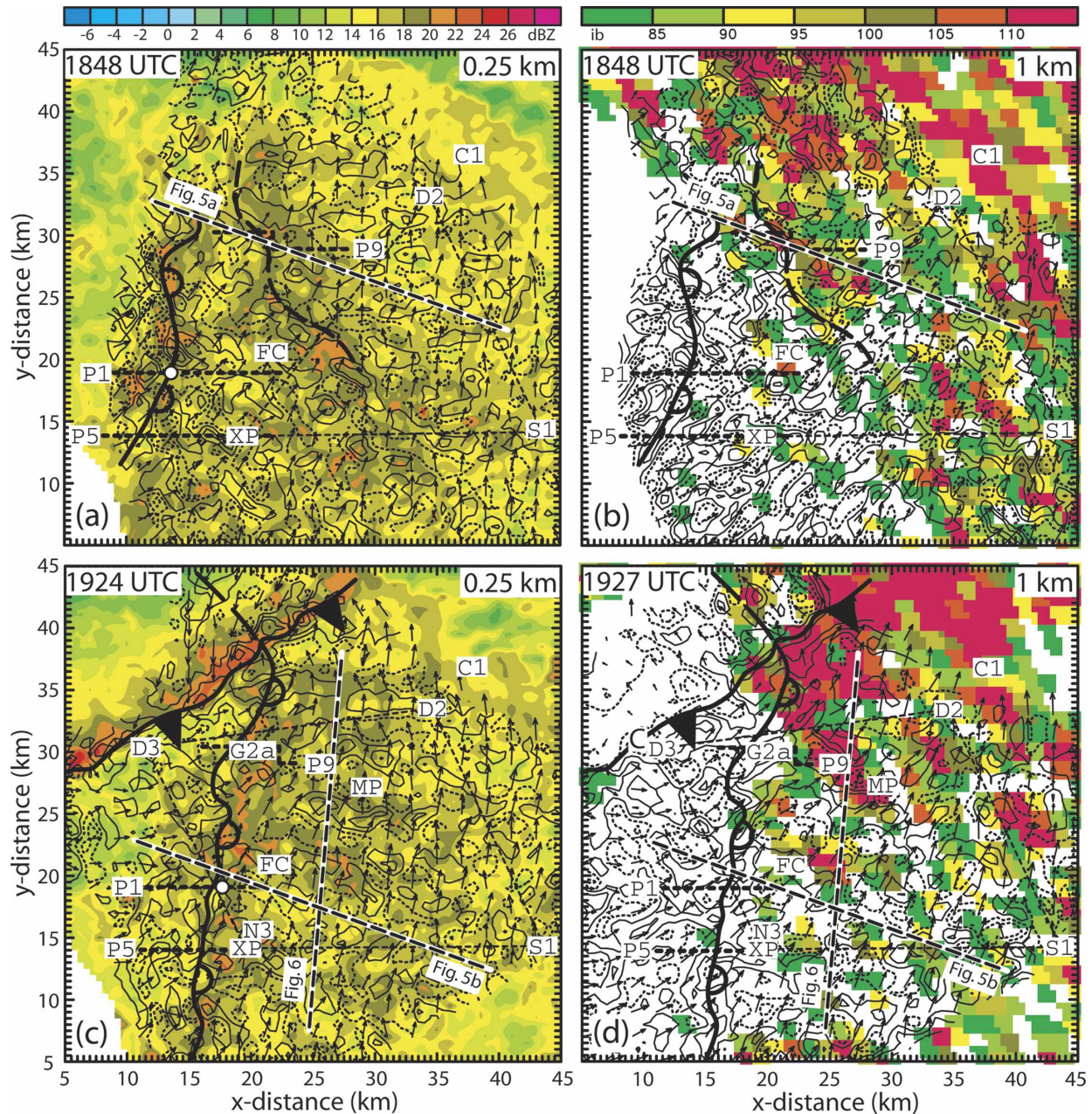


FIG. 3. Comparison of Doppler radar and *GOES-8* satellite analyses on 24 May 2002. (left) Ground-relative wind and color-filled reflectivity (dBZ) at 0.25 km AGL; (right) gridded, color-filled *GOES-8* visible satellite imagery (range 0–255 units) at available times, with ground-relative winds at 1 km AGL on 24 May 2002. (a), (b) 1848 UTC, (c), (d) 1924 UTC radar and 1927 UTC *GOES*/winds, (e), (f) 1945 UTC radar and 1942 UTC *GOES*/winds, and (g), (h) 2006 UTC. The cold front, dryline, and a convergence line are denoted by thick solid curves with triangles or scallops and a thick dashed curve, respectively. Boundary locations are deduced from some combination of the nearest available Lagrangian analysis (i.e., if within  $\pm 6$  min), in situ traverses and extension of gradients along streamlines (e.g., for 1848 UTC analysis), and prominent convergence bands. (left) Vertical vorticity contoured at  $2 \times 10^{-3} \text{ s}^{-1}$  interval, with positive values (solid curve) starting at  $1 \times 10^{-3} \text{ s}^{-1}$  and negative values (dotted curve) starting at  $-1 \times 10^{-3} \text{ s}^{-1}$ . (right) Vertical velocity contoured at  $1 \text{ m s}^{-1}$  interval, with positive values (solid curve) starting at  $0.5 \text{ m s}^{-1}$  and negative values (dotted curve) starting at  $-0.5 \text{ m s}^{-1}$ . Thick dotted lines are locations of transects by mobile mesonets P1, P5, and P9; also S1 = SR1, D2 = DOW2, D3 = DOW3, XP = XPOL, FC = field coordinator, N3 = M-CLASS, G2 = M-GLASS2, MP = MIPS, and C1 = cloud camera. Horizontal velocity vectors are scaled by  $1 \text{ km} = 4 \text{ m s}^{-1}$ . Long-dashed lines locate vertical cross sections described in the text. Thin dashed curves labeled GW indicate locations of inferred internal gravity waves described in the text. The white-filled circle in (c) locates P1's 1929 dust devil observation. The dashed boxes in (e) and (f) locate the subgrid shown in Fig. 11. Color-bar label *ib* denotes satellite image brightness scale (Ziegler et al. 2007).

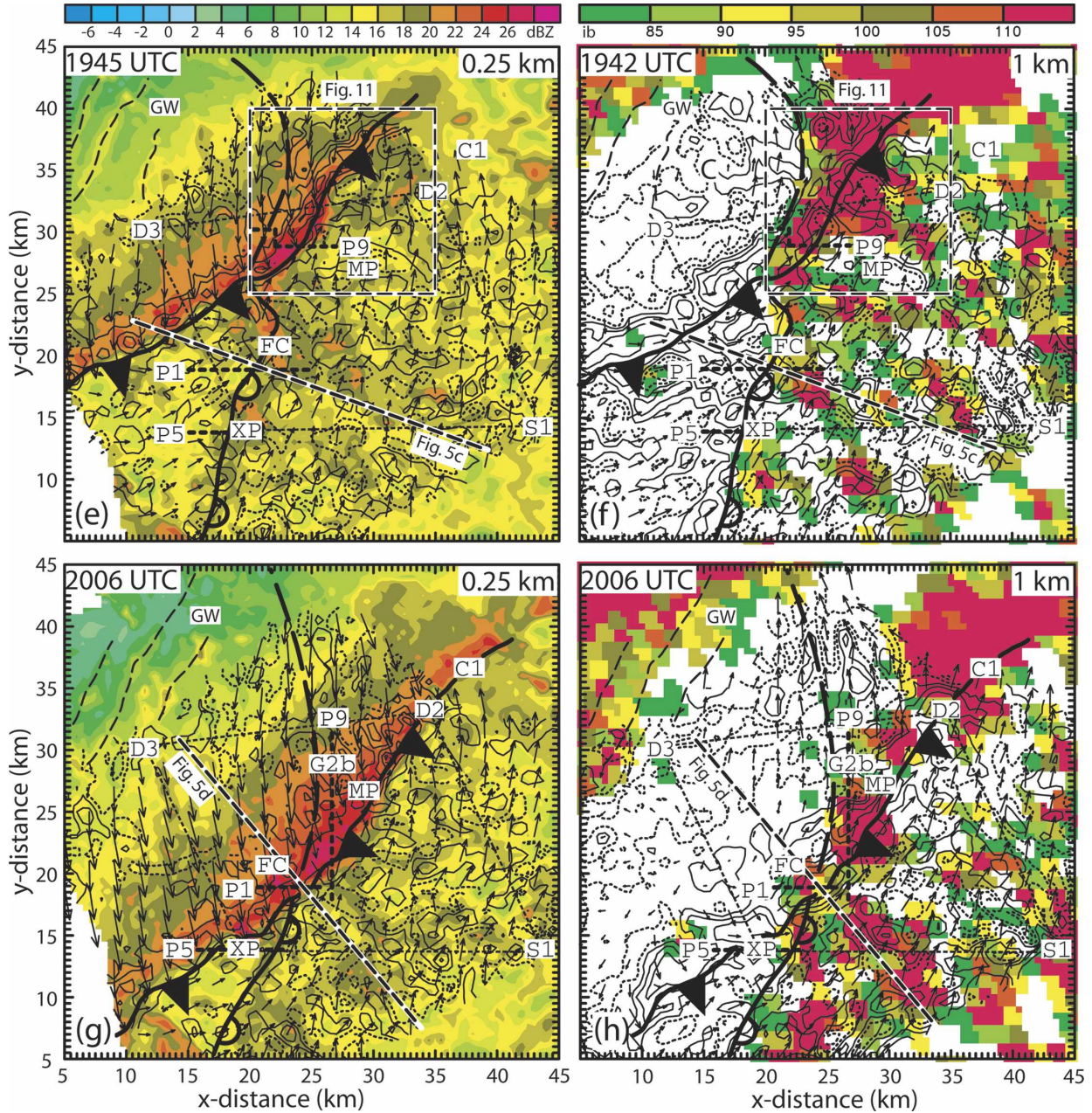


FIG. 3. (Continued)

and interpolated to a subdomain of the radar analysis grid employing a two-pass Barnes spatial and temporal interpolation scheme (Barnes 1973; Ziegler et al. 2007). In the 24 May case, the subdomain dimensions are 25 km in each horizontal direction and 2.5 km vertically. Lateral boundary conditions are imposed from the air-mass-specific reference soundings via forward trajectories from lateral boundary points. Gridpoints with height  $z > z_{LCL}$  have achieved water saturation, implying the presence of cumulus cloud. Areal cumulus coverage from the Lagrangian analysis is validated with

photogrammetric cloud base analyses (e.g., Rasmussen et al. 2003) and gridded Geostationary Operational Environmental Satellite (*GOES-8*) visible images following methods described by Ziegler et al. (2007), while selected local Lagrangian analysis profiles are compared directly with observations reported by G06 and K06.

**3. Radar and in situ data analysis results**

On the afternoon of 24 May 2002, the armada of mobile ground-based and airborne platforms observed

a rapidly moving cold front and its triple point dryline intersection west of Shamrock, Texas, in the eastern Texas panhandle (Fig. 2). Despite convective potential, storms did not develop in the  $\sim 50 \text{ km} \times 50 \text{ km}$  intensive observing region that was targeted for focused mobile IHOP field observations (W06). However, cumuli developed along and ahead of the cold front and dryline (Fig. 2a), while a line of storms developed from west Texas northeastward into western Oklahoma later in the afternoon (e.g., Fig. 2b).

#### a. Doppler analysis and cloud field

The dryline and a convergence line are observed by the mobile radars and mobile mesonets at 1848 UTC (Fig. 3a), while the cumulus cloud field is concentrated northeast of the convergence line (Fig. 3b). A strong cold frontal shearing zone marked by high values of vertical vorticity and reflectivity moves rapidly southeastward through the IOR during the period of radar observations, passing DOW3 between 1924 and 1945 UTC (Figs. 3c,e) and passing the FC just prior to 2006 UTC (Fig. 3g). At 1959, the FC observers note a "... large dust column 1 km east ... near [the] triple point," while at 2000 UTC the "... cold front is passing FC" accompanied by strong gusty winds and the cold front passes the MIPS around 2006 UTC (Figs. 3g,h, 16; K06). The dryline moves slowly eastward between 1848 and 2006 UTC, marked by veering winds and slightly enhanced reflectivities greater than 20 dBZ. In contrast, the highest reflectivities of over 25 dBZ are observed along and just behind the cold front. The FC observers note airborne straw and small leaves in addition to blowing dust following frontal passage, suggesting that postfrontal reflectivities may be significantly enhanced by these large particulate scatterers. Combined with the rapid southward movement of the cold front, the classical triple point intersection of the dryline and cold front moves southward after 1924 UTC (Figs. 3c,e,g).

The cumulus field is concentrated to the east of the dryline and cold front after 1924 UTC (Figs. 3d,f,h), with a broad band of brighter cloud tops developing along the front northeast of the triple point. The western edge of the bright cloud band extends north of the cold front and triple point roughly along the axis of the dryline aloft (Figs. 3d,f,h), implying advection of the predryline air mass and the dryline gradient itself over the front as previously suggested by Weiss and Bluestein (2002). The hypothesis that the dryline gradient is preserved following postfrontal advection is also supported by the Lagrangian analysis results to be shown (e.g., Figs. 14 and 15). However, the northern and western extremity of the cloud field becomes pro-

gressively more ragged in appearance with increasing distance north of the front, implying the action of a dissipative process (e.g., shearing deformation and mixing, subsidence, and evaporation). The southeast edge of the postfrontal stratus cloud shield (Fig. 2a) develops bands coincident with roll-like reflectivity features probably associated with Kelvin–Helmholtz rolls (to be discussed in section 4a) or gravity waves (Figs. 3e–h; see also G06).

The radar analyses reveal finite-length bands of positive and negative vertical vorticity oriented at a large angle to the flow (transverse vorticity bands) ahead of the cold front, and numerous misocyclones are also analyzed in all three air masses (Figs. 3a,c,e,g). Several attachment points of transverse vorticity bands with the cold front are evident [e.g., (17, 35), Fig. 3c; (25, 31), Fig. 3e; (23, 16) and (31, 23), Fig. 3g]. Animations of the 3-min analyses over the 2-h analysis period indicate that individual updraft and reflectivity cores, misocyclones, and transverse vorticity bands ahead of the front all are rather coherent and move steadily with the local horizontal wind (e.g., approximately from the southwest at  $5 \text{ m s}^{-1}$ ). Time sequences of various fields at fixed heights reveal the linear translation of reflectivity cores (Fig. 4a), misocyclones (Fig. 4b), and updraft cores (Figs. 4c,d) with the local low-level flow, demonstrating that these boundary layer features may persist for up to 30 min or more as they move downstream. Interestingly, several reflectivity cores are embedded and move northeastward within the southeastward-advancing frontal surface (Fig. 4a). The differential motions of the front and individual prefrontal vorticity cores are consistent with the previously mentioned attachment of vorticity bands to the cold front.

At 1848 UTC, individual mobile mesonet traverses are used to help locate the dryline and convergence line in zones of enhanced vertical motion, vertical shear, and reflectivity plumes (Fig. 5a). Strong updrafts, collocated reflectivity plumes, and enhanced vertical shear mark the dryline as it moves eastward between 1924 and 1945 UTC (Figs. 5b,c). Several BL circulations are evident on either side of the dryline (e.g., at  $x = 15.5 \text{ km}$ , Fig. 5a;  $x = 5, 20 \text{ km}$ , Fig. 5b;  $x = 20 \text{ km}$ , Fig. 5c), indicating the presence of rolls oriented along the low-level southerly flow (i.e., longitudinal rolls). The sloping cold front is marked by strong updrafts, vertical vorticity up to  $5 \times 10^{-3} \text{ s}^{-1}$ , and a deep reflectivity plume along and rearward of its leading edge at 1945 and 2006 UTC (Figs. 5c,d). GOES-8 images projected into the cross sections indicate that clouds are present above and downstream from updraft cores, though not all updrafts form clouds. Since individual misocyclones

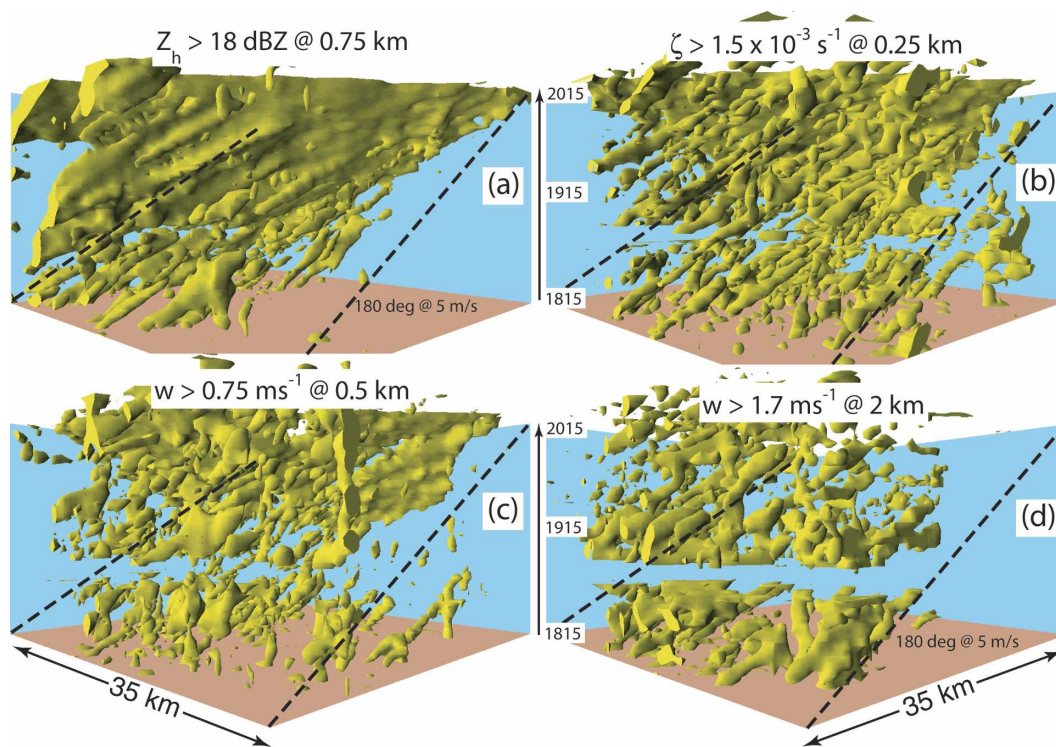


FIG. 4. Constant value 3D perspective surface plots at indicated height (i.e., 2D constant-level vs time) depicting the evolution of selected radar analysis parameters during the period 1815–2015 UTC on 24 May 2002. (a) reflectivity (18 dBZ at 0.75 km); (b) vertical vorticity ( $1.5 \times 10^{-3} \text{ s}^{-1}$  at 0.25 km); (c) vertical velocity ( $0.75 \text{ m s}^{-1}$  at 0.5 km); (d) vertical velocity ( $1.7 \text{ m s}^{-1}$  at 2 km). Dashed black reference lines indicate a Lagrangian motion from  $180^\circ$  at  $5 \text{ m s}^{-1}$ . The red bottom surface corresponds to the initial time, while the blue side panels are the  $(x, t)$  and  $(y, t)$  lateral bounding surfaces of the domain.

exhibit a degree of quasi-steadiness in a vortex-relative reference frame (e.g., Fig. 4b), the transient vorticity cores in the spatial cross sections are actually due to the aforementioned motion of mesocyclones and vorticity bands into the plane. A pronounced roll circulation coincides with the reflectivity plume just behind the surface cold frontal position (Fig. 5d; see also W-band radar analysis in Fig. 10b of G06), accompanied by intense upper-level diffluence and a sloping front-relative rearward flow and a high-reflectivity layer that approximately conserves reflectivity following the motion (Figs. 5d and 3d,f,h).

The previously noted transverse vorticity bands are associated with transverse BL rolls (their possible physical forcing mechanisms to be discussed in section 4). A series of transverse rolls spaced about 4–5 km apart move steadily northeastward, distinguished by persistent vorticity and vertical velocity extrema and reflectivity plumes in updrafts (Fig. 6). For example, a well-defined roll (core 3, Fig. 6) maintains the amplitude of its collocated updraft and reflectivity plumes and the flanking opposite-sign vertical vorticity centers

between 1912 and 1936 UTC. The association between upward and downward oscillations of airflow in the plane with undulations of a reference (positive) normal velocity contour and associated vertical vorticity cores suggests that the transverse rolls generate along-axis vertical vorticity by tilting and stretching the westerly boundary layer shear (i.e., the shear component parallel to the roll axis). The transverse vorticity bands are finite length (Figs. 3a,c,e,g), supporting the speculation that the longitudinal and transverse roll modes coexist but destructively interfere. Satellite imagery suggests that clouds are located above and downstream from updraft cores and move with the rolls (Fig. 6).

The longitudinal and transverse rolls are frequently distinguished by reflectivity plumes in their updrafts (Figs. 5–6). However, reflectivity maxima are also noted in downdrafts contained in selected cross sections due to advection of scatterers downstream into the plane from an adjacent finite-length longitudinal roll updraft and its associated reflectivity plume. The existence of BL reflectivity plumes (i.e., caused by microinsects) is consistent with the ambient stratification of

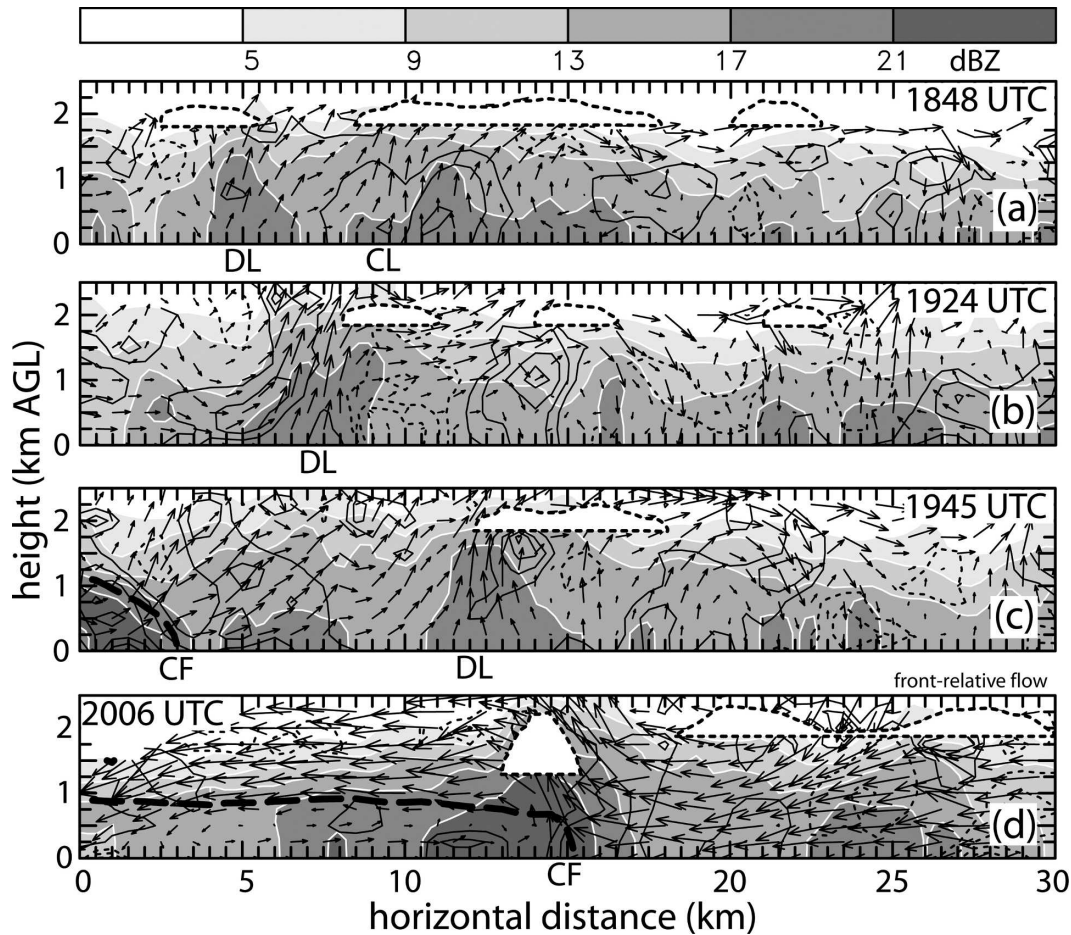


FIG. 5. Doppler-derived wind and reflectivity in boundary-normal vertical cross sections on 24 May 2002, oriented as in Fig. 3. (a) 1848, (b) 1924, (c) 1945, (d) 2006 UTC. (a)–(c) Winds are ground-relative, while winds in (d) are relative to the cold frontal motion from  $315^\circ$  at  $6.4 \text{ m s}^{-1}$ . Gray fill is reflectivity (dBZ). Black curves are vertical vorticity contoured at  $1 \times 10^{-3} \text{ s}^{-1}$  interval, with positive values (solid curve) starting at  $1 \times 10^{-3} \text{ s}^{-1}$  and negative values (dotted curve) starting at  $-1 \times 10^{-3} \text{ s}^{-1}$ . Velocity vectors are scaled by  $1 \text{ km} = 7 \text{ m s}^{-1}$ . Long-dashed curve in (c), (d) is zero normal horizontal flow component (i.e., with positive values into the plane above and smaller or negative values below). White-filled dotted curves denote clouds inferred from *GOES-8* imagery in the cross section (Figs. 3b,d,f,h), assuming a flat cloud base at the local sounding LCL of 1.8 km (1.2 km at 2006 UTC along the cold front). Cloud tops (i.e., thickness) are proportional to *GOES-8* image brightness with adjustments for KA in situ cloud penetration altitudes. Off-time satellite images are locally advected to the cross section assuming a cloud motion of  $60^\circ$  at  $10 \text{ m s}^{-1}$ . Labels DL = dryline, CF = cold front, and CL = convergence line boundary.

reflectivity and the notion that radar scatterers move approximately as passive tracers (i.e., as moisture) with terminal velocities substantially smaller than (though possibly in proportion to) peak updrafts (Geerts and Miao 2005).

The frontal and dryline characteristics from the present ground-based radar analyses are qualitatively compared with the airborne pseudodual Doppler analysis of W06 in the area where the respective analysis domains overlap (Fig. 2a). Although the frontal and dryline shears and reflectivity maxima are broadly comparable (e.g., Fig. 4 of W06 versus Figs. 3c–h), the peak

vertical vorticity values of the present analysis are roughly 2–3 times the magnitude of the pseudodual Doppler analysis values due to the finer time and space resolution and smaller filtering of the ground-based radars. For example, a transverse vorticity band attached to the frontal shear zone in the present analysis at (17, 35) and 1924 UTC (Fig. 3c) is revealed as a southeastward-extended lobe of the main frontal vorticity maximum in the 1915–1927 UTC pseudodual Doppler analysis (Fig. 4a of W06). However, the longitudinal and transverse roll updrafts to the east of the front and dryline are discernable only in the present analysis.

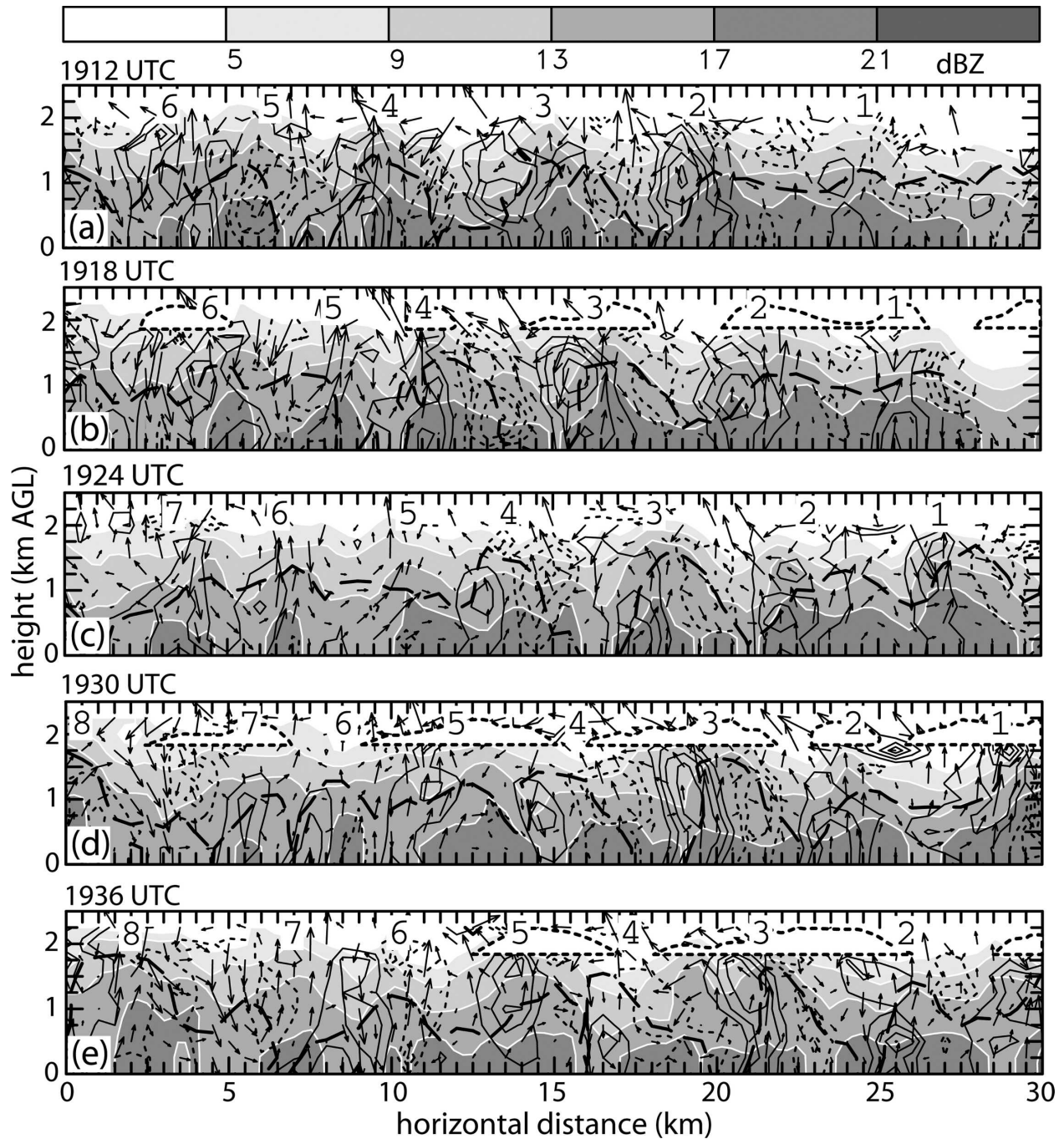


FIG. 6. Doppler-derived wind and reflectivity in a vertical dryline-parallel cross section on 24 May 2002 as in Fig. 5 (oriented in Fig. 3): (a) 1912, (b) 1918, (c) 1924, (d) 1930, (e) 1936 UTC. Velocity vectors are relative to an assumed motion from  $185^\circ$  at  $5 \text{ m s}^{-1}$ , with magnitude scaled by  $1 \text{ km} = 5 \text{ m s}^{-1}$ . Long-dashed curve is  $2 \text{ m s}^{-1}$  normal horizontal flow component out of the plane (i.e., with larger values out of the plane above and smaller or negative values below). Clouds are depicted as in Fig. 5 relative to available GOES-8 images at 1918, 1928, and 1935 UTC.

*b. Mobile mesonet analysis*

Low-speed dryline traverses by mobile mesonets (i.e., probes) P1, P5, and P9 provide up to 20 m along-leg spatial resolution profiles from 1833 to 1955 UTC

(Fig. 7). One or more dryline vapor mixing ratio gradients are observed on each leg, with widths of 0.5–1 km and magnitudes of up to  $3 \text{ g kg}^{-1} \text{ km}^{-1}$ . The observed dryline movement is variable, with multiple cycles of an eastward surge followed by a short period of near-

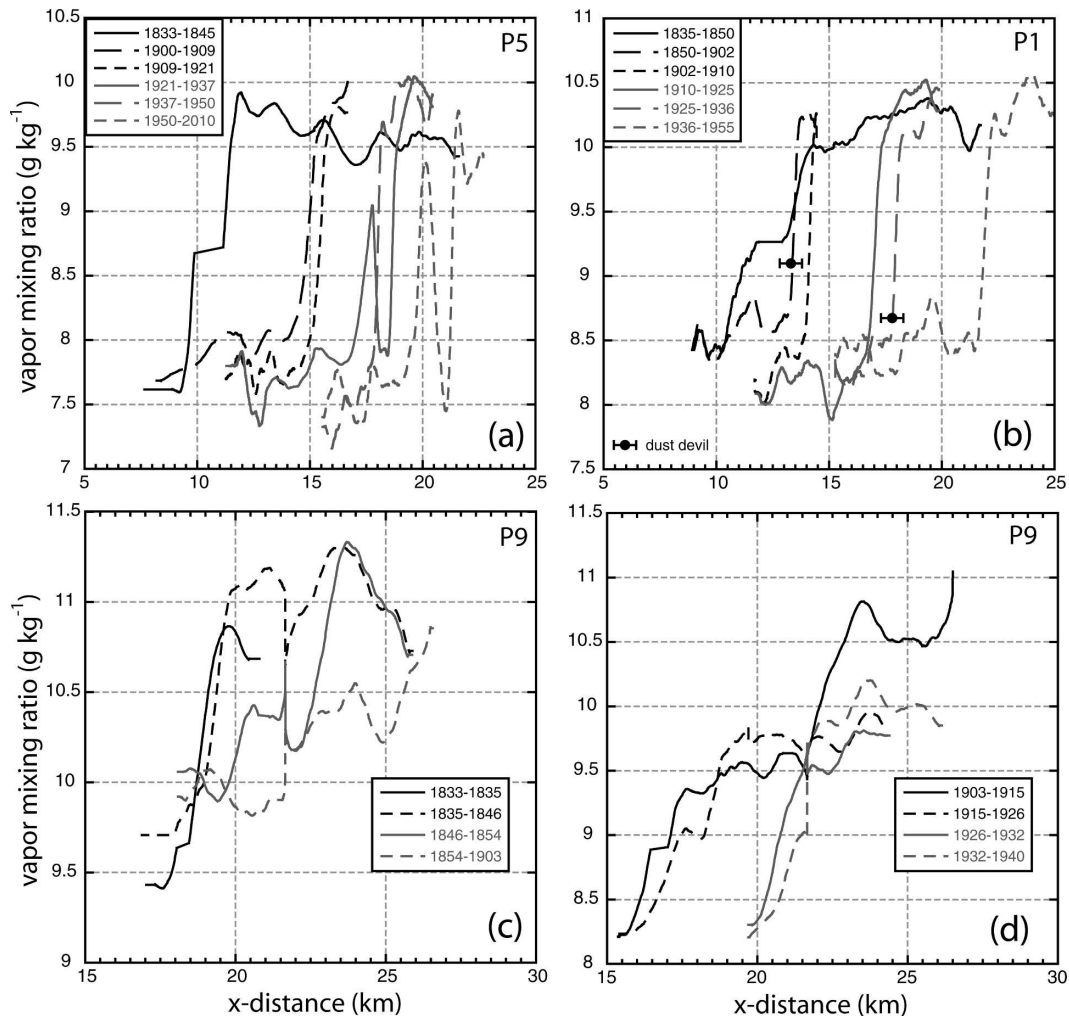


FIG. 7. Profiles of vapor mixing ratio ( $\text{g kg}^{-1}$ ) along dryline traverses on 24 May 2002. In order from south to north along the dryline (as located in Fig. 3): (a) probe 5, (b) probe 1, (c) probe 9 (early traverses), (d) probe 9 (late traverses). Note the different vertical scales in each panel. A dot-and-whiskers symbol locates an estimated dust devil location and its positioning uncertainty based on visual reports logged by the mobile mesonet crew.

stationarity observed by probes P5 (Fig. 7a) and P1 (Fig. 7b) and an east–west oscillation observed by P9 (Figs. 7c,d). Considering the southwesterly wind and the dryline orientation at the locations of traverses (Fig. 3), the observed dryline displacements are consistent with wavelike perturbations moving northward along the dryline. Here, P1 and P5 observe maxima of virtual potential temperature along or east of the dryline, with winds veering west of the dryline (Figs. 8a,b); P9 observes a double dryline (e.g., Ziegler and Hane 1993) with gradients of moisture, virtual temperature, and veering winds centered at  $x = 17$  and  $x = 22$  km (Fig. 8c).

Selected frontal traverses by the mobile mesonets reveal rather complex horizontal thermal gradients on

both sides of the cold front around the triple-point intersection. Moisture minima just ahead of the cold front indicate that P1 and P5 traverse the front to the south of the triple point, while P9 traverses the cold front to the north of the triple point (Figs. 8d–f). The sharp temperature drop associated with the cold front is preceded by a narrow zone of sharply veering winds (Figs. 8d–f). While potential temperature decreases west of the moisture rise marking the front (not shown), the virtual potential temperature profile just behind the front may either decrease (Figs. 8d,f) or remain unchanged (Fig. 8e) depending on the relative magnitudes of the initial temperature decrease and moisture increase.

Dust devils are observed near the dryline ahead of P1

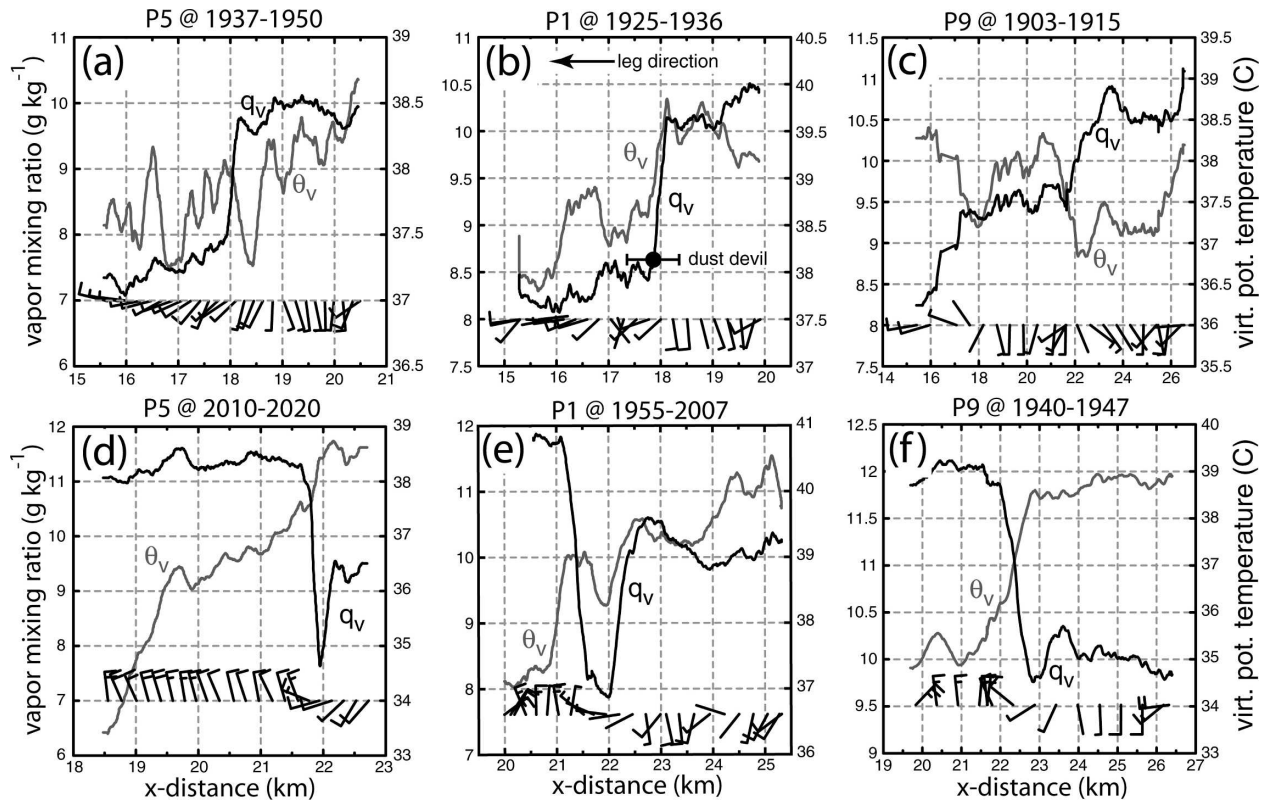


FIG. 8. As in Fig. 7, but showing profiles of horizontal wind, vapor mixing ratio ( $\text{g kg}^{-1}$ ), and virtual potential temperature ( $^{\circ}\text{C}$ ) on selected boundary-crossing mobile mesonet traverses on 24 May 2002. (a)–(c) Dryline traverses, (d)–(f) cold frontal traverses. Full and half wind barbs equal 5 and  $2.5 \text{ m s}^{-1}$ , respectively, while a nonbarbed wind is less than  $1 \text{ m s}^{-1}$ .

during its 1850–1902 and 1925–1936 UTC traverses (Figs. 3a,c). The dust devils are located within the dryline moisture gradient (Figs. 7b, 8b), the later dust devil occurring in a zone of sharply veering winds. Using a time-to-space adjustment of the dust devil locations relative to the closest radar analysis to confirm dust devil location in a zone of radar-derived wind shear (not shown), it is speculated that the dust devils or their parent misocyclones may form via a horizontal thermal-shearing instability (Kanak et al. 2000). Other mobile mesonets also report dust devils along or near the dryline, although their timing and location are not reported with sufficient accuracy to position them with respect to the analysis grid.

### c. Ground-based mobile soundings

Ground-based mobile soundings are obtained behind the cold front (Fig. 9a) and at two locations on the dryline (Figs. 9b,c). A well-mixed BL that is absolutely unstable to dry convection (i.e., the convective BL or CBL) is present along the dryline, with conditions slightly warmer and drier at the northern location (Fig.

9b) than 15 km to the south (Fig. 9c). The southern dryline sounding is convectively unstable, with a convective available potential energy (CAPE) of  $1152 \text{ J kg}^{-1}$ , and moderately capped with a convective inhibition (CIN) of  $59 \text{ J kg}^{-1}$ . A second M-CLASS sounding at 2056 UTC east of the IOR (not shown), though similar to the 1920 UTC M-GLASS sounding (Fig. 9b), has slightly deeper BL moisture and zero CIN. The post-frontal 2006 UTC M-GLASS sounding (Fig. 9a) contains a shallow CBL topped by a strong frontal inversion. An elevated residual layer (ERL) in the soundings proceeds from the transport of the deep, dry CBL between the surface dryline and cold front by horizontal and vertical advection relative to the surface boundaries. Cumulus development on the northern portion of the dryline (Fig. 3d) is assisted by a shallow layer of weak instability just above cloud base in the 1920 UTC M-GLASS sounding (Fig. 9b inset), while the other soundings are stable at all levels in the cloud-bearing layer. Reference soundings for the three air masses (Fig. 9d) are derived from the mobile soundings and a King Air stepped traverse analysis (Ziegler et al. 2007).

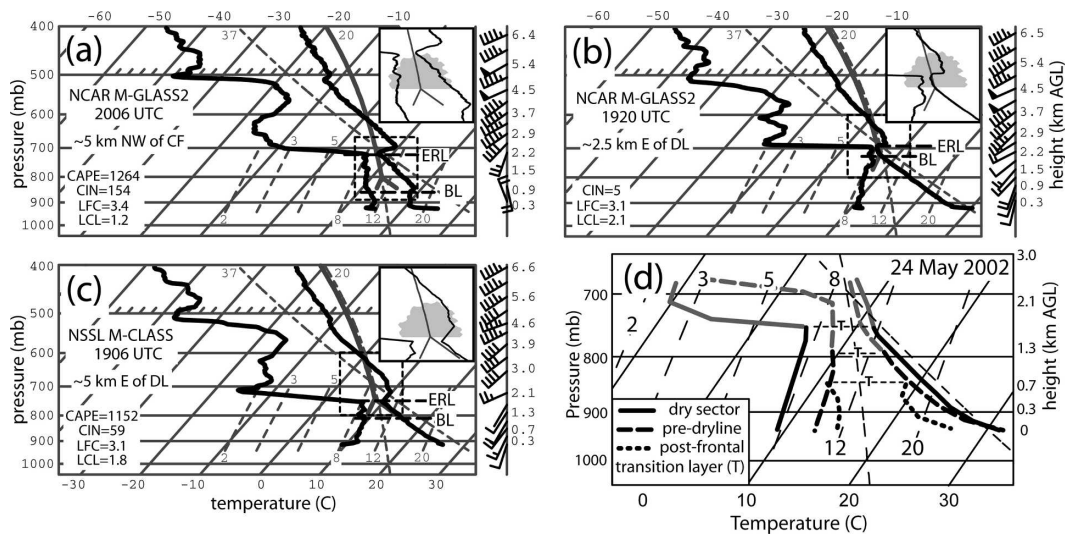


FIG. 9. Mobile ground-based and reference soundings on 24 May 2002 (located in Fig. 3). (a) NCAR M-GLASS2 (G2b) at 2006 UTC (5 km northwest of cold front); (b) NCAR M-GLASS2 (G2a) at 1920 UTC (2.5 km east of dryline near triple point); (c) NSSL M-CLASS unit (N3) at 1906 UTC (5 km east of dryline and 25 km south of triple point); (d) boundary layer reference soundings (adapted from Ziegler et al. 2007). Wind barbs are plotted as in Fig. 8. Inset shows sounding detail overlaid on a hypothetical 1-km-deep cumulus cloud. Label T = transition layer while labels BL and ERL are defined in the text.

#### d. Surface Lagrangian moisture analysis

The surface-level Lagrangian analysis sharply delineates the evolving dryline and cold front and defines the areal coverage of moisture necessary for cloud development (Fig. 10). An axis of weak along-dryline confluence provides frontogenetic forcing (not shown) to bring individual trajectories into close proximity, thus maintaining the dryline moisture gradient as observed by mobile mesonet traverses in the analyses. The pre-dryline, dry sector, and postfrontal air masses are characterized by vapor mixing ratios of 9–10, 7–8, and 11–12  $\text{g kg}^{-1}$ , respectively (see also Figs. 7–8), while MIPS time series changes (K06) are consistent with the rapid southeastward frontal movement combined with analyzed cross-frontal gradients at the MIPS site (e.g., Fig. 10h). The triple point moves southward after 1933 UTC due to the rapid southeastward frontal movement combined with slow eastward dryline motion. The dryline develops undulations with spacings of 5–15 km, consistent with the previously mentioned dryline oscillations inferred from mobile mesonet traverses. Similar dryline undulations have been inferred by McCarthy and Koch (1982), prompting them to propose the term mesoscale dryline wave to describe this phenomenon. Intense convergence and shearing provide the frontogenetic forcing (not shown) to maintain a strong moisture gradient across the cold front.

A series of persistent longitudinal moisture bands spaced 1–5 km apart are located to the east of and

roughly parallel to the dryline (Fig. 10). The longitudinal moisture bands are approximately stationary or may vacillate slightly in the cross-flow direction. Other longitudinal moisture bands are located west of the dryline and are aligned along confluence bands (e.g., moisture band southwest of P2; Figs. 10a–c). Pockets of drier air form west of the dryline between the moisture bands, locally increasing the horizontal moisture gradient across the dryline. The location of P1's 1929 UTC dust devil observation is along the dryline and just northeast of the advancing dry pocket located to the west of P4 (Fig. 10c).

An important capability of the Lagrangian analysis is the derivation of the LCL height field. Surface parcels at 1942 UTC in the sharply contrasting predryline, dry sector, and postfrontal air masses have LCL values of about 1.8–2, 2.2–2.8, and 1.2–1.4 km, respectively (Fig. 10f), the dry air mass having the greatest heterogeneity. The postfrontal and predryline LCL height values are broadly consistent with layer-averaged LCL heights from the mobile soundings (Fig. 9).

### 4. Boundary layer roll updrafts in relation to cumulus and storm development

#### a. Roll dynamics

The previously noted transverse rolls (Figs. 3 and 6) appear to be consistent with the inflection point instability (e.g., Stensrud and Shirer 1988), which is related to the Kelvin–Helmholtz instability. Generally BL rolls

can be produced by three types of instability (Brown 1980): 1) thermal instability, the combination of Rayleigh–Benard convection with horizontal flow in which the most unstable orientation minimizes cross-roll shear (e.g., longitudinal rolls on either side of the dryline in Fig. 5); 2) parallel instability, in which roll circulations extract energy from the mean shear parallel to the roll axis via the Coriolis force (Lilly 1966); and 3) inflection point instability, in which rolls extract energy from the BL shear normal to the roll axis. The growth rate of the inflection point instability is proportional to the magnitude of the shear at the inflection point (Brown 1980). Depending on the BL shear profile, the inflection point instability may generate a variety of roll orientations which often differ from the roll orientations produced by either the thermal or parallel instabilities. Depending on the degree of shear and unstable stratification in the BL, a most-unstable mode of both the inflection point and thermal instabilities may coexist (Gossard and Moninger 1975).

An inflection point was identified in the high-resolution BL wind profile (i.e.,  $\sim 50$ -m altitude spacing at  $\sim 5 \text{ m s}^{-1}$  rise rate for 10-s interval data) of the 1906 UTC M-CLASS sounding (Fig. 9c), establishing the necessary (but not sufficient) condition for inflection point instability. The low-order spectral model of Stensrud and Shirer (1988) verified the existence of inflection point instability in the input 1906 UTC M-CLASS sounding. With input of the observed roll spacing of 5 km and the assumption that roll depth equaled the BL depth of 1.25 km, the low-order spectral model was used to estimate the orientation of the most unstable mode as  $275^\circ$ . This computed orientation is in favorable agreement with the roll orientation suggested by Fig. 3. The cross section in Fig. 6 has been rotated to be orthogonal to the most unstable mode's orientation to better reveal the roll structure. Consistent with the sounding, the mean Doppler-derived horizontal wind component profiles in each cross section in Fig. 6 were calculated and found to further support the existence of an inflection point in the BL. In contrast to the linear analysis of Gossard and Moninger (1975) that assumed a straight hodograph and obtained a 2D dynamical (inflection point) solution lacking perturbation vertical vorticity, the observed transverse rolls in the present study appear to produce vertical vorticity banding due to the observed turning wind with height and tilting of the associated along-roll shear component.

#### b. Comparison of GOES-8 and cloud camera analyses

Good internal consistency is found between *GOES-8* cloudiness and cumulus cloud base areas derived from

the photogrammetric analysis (Fig. 11). Individual cloud base centers move approximately with the subcloud winds, initially northeastward ahead of the cold front and then northward as subcloud winds back in response to the solenoidally induced secondary cold frontal vertical circulation (see also Figs. 3e,f and 5d). Cloud bases were analyzed at a 90-s interval (Ziegler et al. 2007), and animations reveal the regularity of the cloud-base motions. Roughly 50% of the cloud-base areas are forced or active clouds situated in updraft below the LFC (Stull 1985). The total cloud base area is 25%–50% of the total cloud-top area, consistent with the notion of the cumuli as detraining plumes that broaden with height.<sup>3</sup> An evolution is suggested in which clouds initiate at the centers or on the downwind edges of updrafts (as also concluded from MIPS observations by K06), followed by advection of the cloud bases over areas with either weaker updrafts or downdrafts. Thus, clouds exhibit both active and inactive periods in their individual evolutions. In broad consistency with the previously noted persistent movement of updrafts near the LCL height (Fig. 4d), some cloud bases persist for periods of at least 12–21 min (e.g., cell 2 in Figs. 11a–c; cell 5 in Fig. 11a–d).

The photogrammetric and radar analyses further emphasize the role of vertical circulations associated with BL updraft cells and the cold front in forcing cumulus development (Fig. 12). For example, at 1942 UTC cloud 2 has approximately the same tilt as and is centered within the mesoscale updraft above the frontal location (Figs. 11b, 12a), while at 1957 UTC the bases of clouds 6 and 9 are also embedded in the frontal updraft (Figs. 11d, 12b). Several clouds are in the process of separating from the updraft that formed them (e.g., cloud 1, Figs. 11b and 12a; cloud 4, Figs. 11d and 12b). Cloud 3, having been in updraft at 1936 UTC (Fig. 11a), has separated from its parent updraft (Figs. 11b, 12a) prior to attaching to the frontal updraft at 1948 UTC (Fig. 11c). Cloud 5 follows a similar evolution to cloud 3, except that it is in the process of attaching to the prefrontal BL updraft at 1957 UTC (Figs. 11, 12b).

#### c. Lagrangian boundary layer analysis

The moist boundary layer contains undulations and plumes of vapor mixing ratio, and several plumes achieve water-saturated volumes within which cumulus or cumulus fractus clouds may be inferred (Fig. 13).

<sup>3</sup> Because of limited GOES spatial resolution, inferred cloud cover may be broadened as a result of unresolved cloud holes and edges (e.g., Parker et al. 1986) while mixing-induced breakup into cumulus fractus (e.g., see Fig. 12) would be undetected.

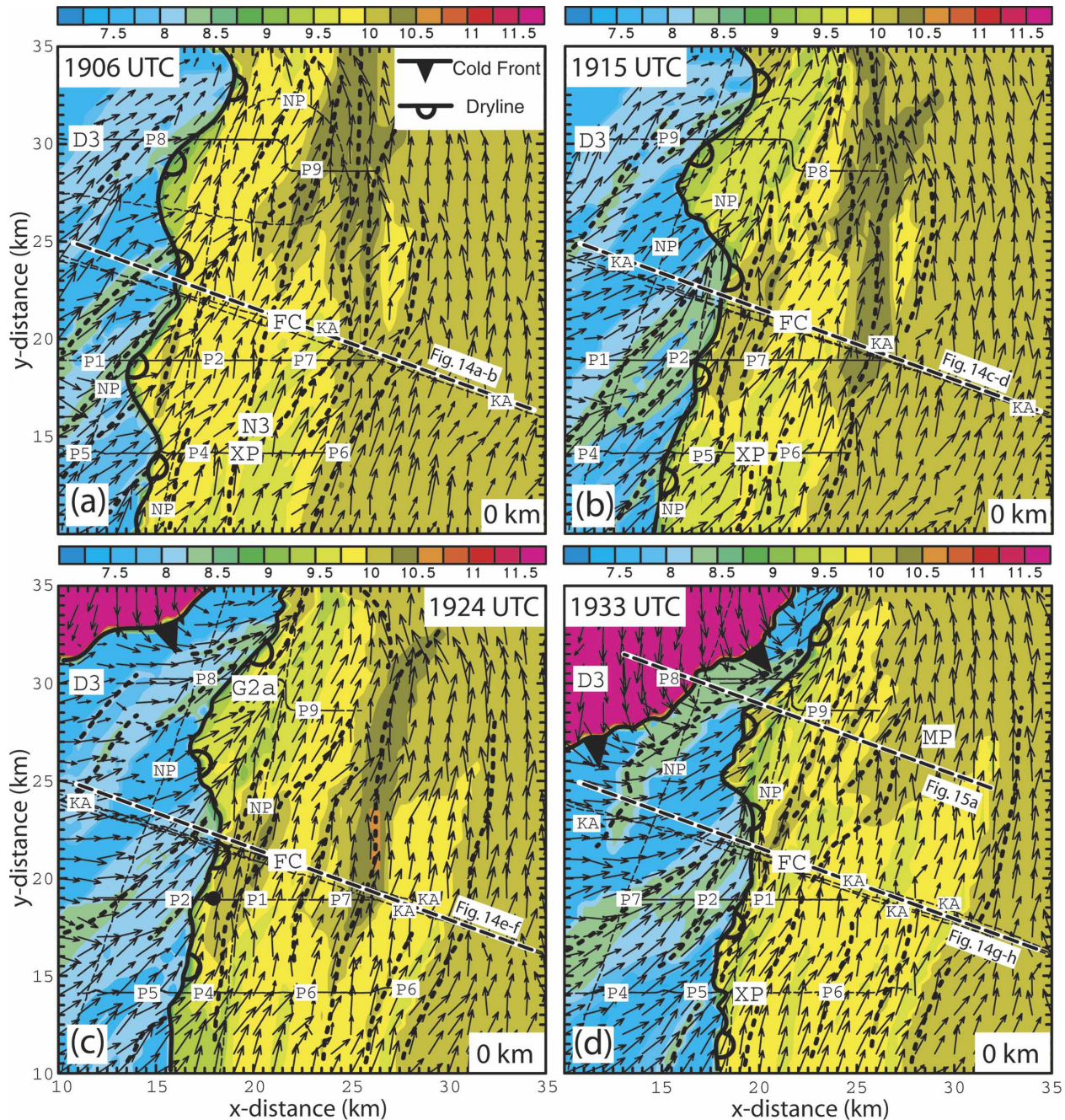


FIG. 10. Surface Lagrangian vapor mixing ratio and ground-relative wind analyses on 24 May 2002: (a) 1906, (b) 1915, (c) 1924, (d) 1933, (e) 1942, (g) 1951, and (h) 2000 UTC. (f) Ground-level LCL height at 1942 UTC. Color scales of vapor mixing ratio ( $\text{g kg}^{-1}$ ) and LCL height (km AGL) are indicated above panels. Every other horizontal velocity vector is plotted with magnitude scaled by  $1 \text{ km} = 4 \text{ m s}^{-1}$ . The thin black dashed lines (with labels denoting platforms) locate mobile mesonet and aircraft traverses employed in each analysis, while thick dashed lines locate vertical cross sections discussed in the text. Platform labels KA = King Air, NP = NRL P-3, while other labels are defined in Fig. 3. Thick dotted curves are inferred moisture bands. The black dot in (c) is the dust devil location previously shown in Figs. 3c and 7b.

These water-saturated volumes are thus complementary to and yet distinct from clouds observed by the ground-based camera or *GOES-8*. The leading edges of the dryline and cold frontal surfaces intersect along a

northeastward-sloping triple point curve. The intense, deep updrafts along the cold front produce a nose of enhanced moisture punctuated by plumes in updraft cores above and slightly rearward of the surface frontal

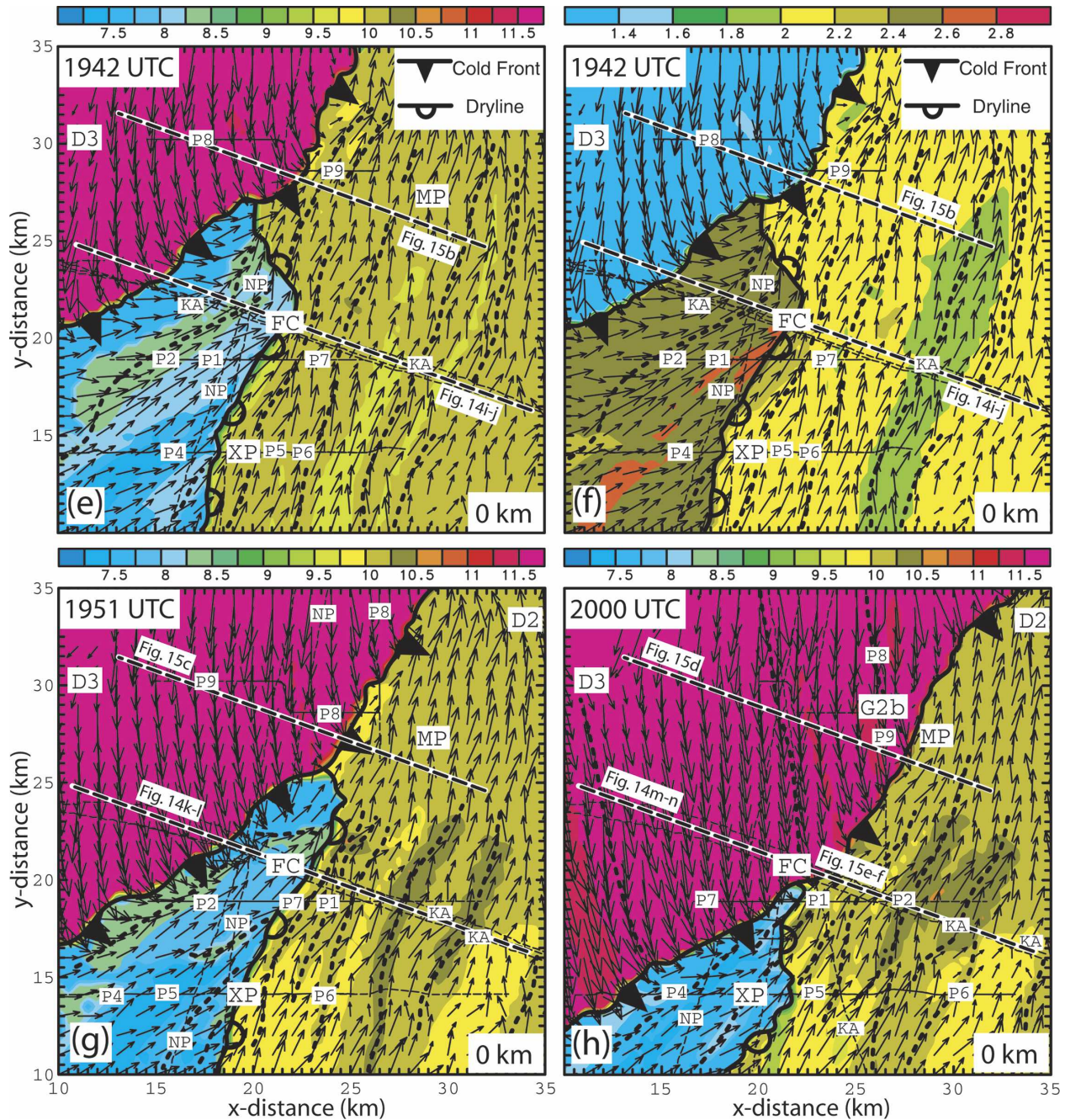


FIG. 10. (Continued)

location. The frontal surface (Figs. 13b–f) displays the convergence-forced nose tilted slightly toward the warm air at several locations, the forward tilt possibly caused by surface friction and suggesting a similarity to density currents (Schultz 2005). The frontal surface also displays a lobe-and-cleft structure suggesting an additional similarity to density currents.

The previously noted plumes east of the dryline co-

incide with updrafts (including longitudinal rolls) that circulate cool, moist air from the top of the BL through the ERL (Fig. 14), developing water-saturated volumes with bases around 1.75 km. The relatively dry, warm, stable layer above the ERL slopes upward in the sheared mesoscale updrafts to the east of the dryline, thereby preventing the saturated volumes from deepening. Although updrafts between the cold front and

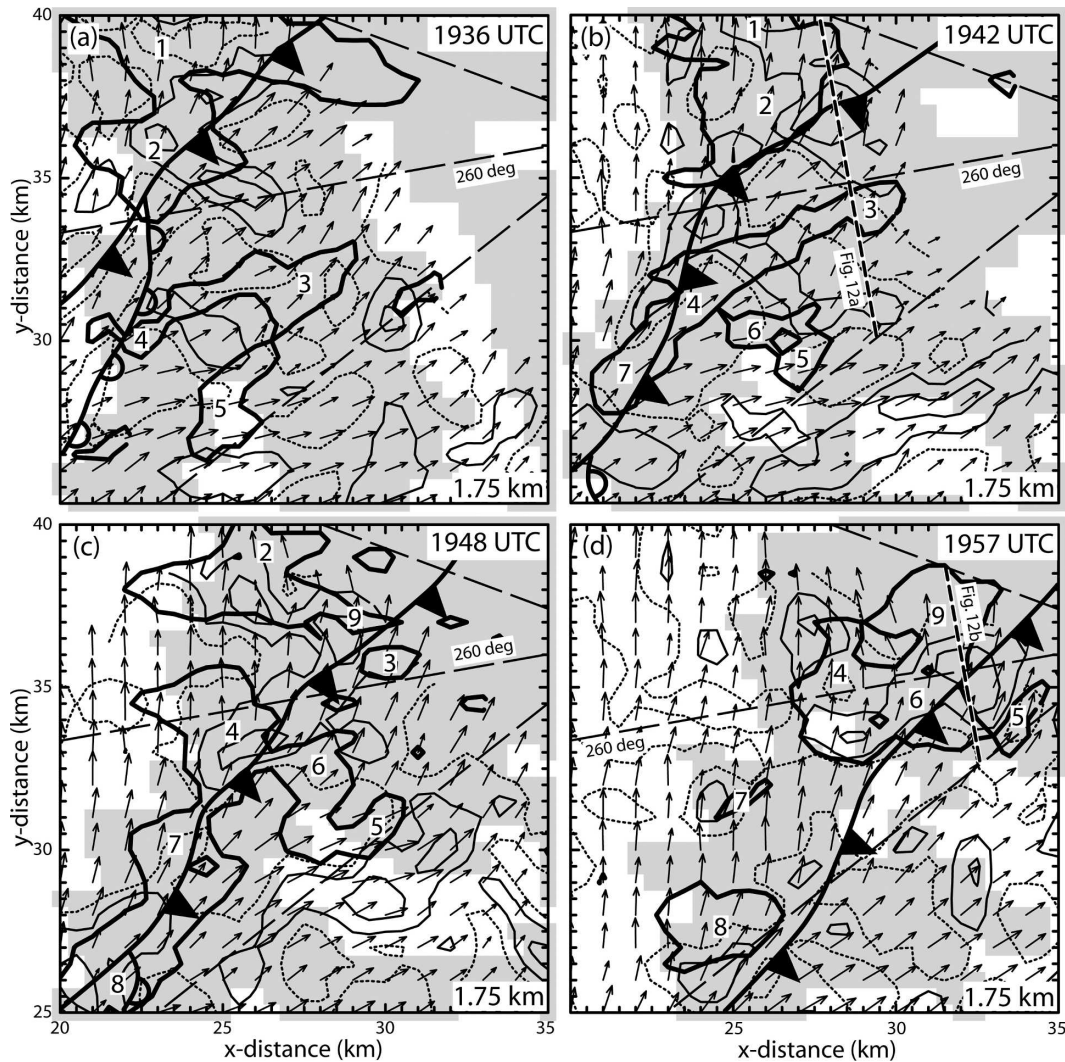


FIG. 11. Cloud-base digital camera and *GOES-8* visible imagery analyses overlaid on ground-relative wind analysis at 1.75 km at (a) 1936, (b) 1942, (c) 1948, and (d) 1957 UTC 24 May 2002. Gray fill denotes grid cells with *GOES-8* brightness > 80 units (0–255 scale), while heavy black curves enclose >50% cloud-base coverage from photogrammetric digital camera analysis (Ziegler et al. 2007). Every other horizontal velocity vector is plotted with magnitude scaled by  $1 \text{ km} = 10 \text{ m s}^{-1}$ . Thin solid contours denote positive vertical velocity at a  $1 \text{ m s}^{-1}$  contour interval starting at  $1 \text{ m s}^{-1}$ , while the dotted contour is zero vertical velocity. Positions of the surface cold front and dryline are inferred from the Lagrangian and radar analyses. Thin, long-dashed unlabelled lines denote azimuthal sector viewed by digital cloud camera, while the central  $260^\circ$  azimuth is labeled. Short-dashed lines locate vertical cross sections described in the text.

dryline tend to be deeper and stronger than updrafts to the east of the dryline, drier air and larger LCL heights (e.g., Fig. 10f) inhibit development of water saturation west of the dryline. Nearly stationary longitudinal rolls west of the dryline produce persistent downward mesoscale entrainment of dry air from above the inversion, resulting in strong heterogeneity of the dry BL prior to cold frontal passage. These deep, longitudinal roll-induced dry intrusions to the west of the dryline are manifested by the previously noted dry bands at the

surface (Fig. 10). A very shallow, cool, and moist CBL behind the cold front is preceded by an upward bulge of postfrontal air in the rotor circulation above the surface frontal location (Figs. 14i–n), thus providing conditions increasingly favoring shallow cumulus formation as the plume depth approaches the parcel LCL height of about 1.25 km (e.g., Fig. 10f).

The predryline and postfrontal BLs exhibit horizontal virtual temperature gradients that support the action of thermally direct secondary circulations. The surface

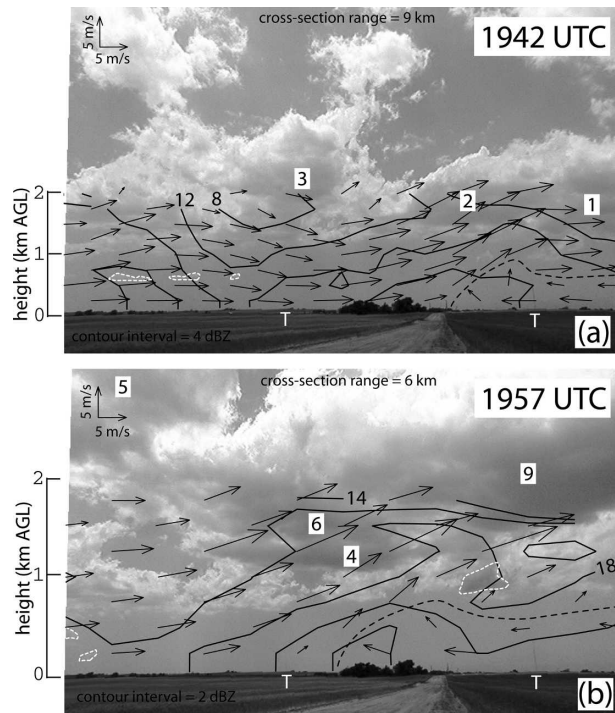


FIG. 12. Digital camera cloud field photographs with overlaid ground-relative radar winds and contoured reflectivity (dBZ) in vertical cross sections located in Fig. 11: (a) 1942 and (b) 1957 UTC. Every other velocity vector horizontally is plotted with magnitude scaled as indicated at upper left. An indicated cross-sectional range is a horizontal distance from the camera along the central  $260^\circ$  azimuth as indicated in Fig. 11. Numbers denote cloud cores near the cross section (i.e., as indicated in Fig. 11). Postfrontal cumulus fractus and cumulus clouds with probable lower bases than prefrontal clouds (outlined by white dashed curves) were masked during photogrammetric analysis of the prefrontal cloud-base areas (Ziegler et al. 2007). Tall tower locations used to correct camera azimuth indicated by T.

dryline associates with a vertical circulation whose updraft is frequently displaced toward the warm, dry side of the dryline (Fig. 14). Cooler virtual temperatures in the predryline and postfrontal BLs (Figs. 14b,d,f,h,j,l,n) imply the sustained generation of horizontal vorticity and vertical shear by a persistent thermally direct solenoid (e.g., Ziegler et al. 1995). However, plumes of rising warm air and sinking cool air in the lowest 1 km modulate both the sign and magnitude of the horizontal temperature gradient in the predryline BL. The postfrontal plume of cold updraft air is similar to the cold frontal hydraulic head feature reported by Shapiro et al. (1985). The unstable stratification in the dry CBL between the cold front and dryline spans the lowest 0.5–1 km (Figs. 14b,d,f,h,j,l), in agreement with a King Air stepped traverse analysis (Ziegler et al. 2007), while the postfrontal BL is unstable in the lowest  $\sim 250$  m (Figs. 14j,l,n).

The secondary cold frontal circulation displaces the dry and moist BLs at the triple point intersection accompanying the dryline occlusion process (Fig. 15). The combination of ceilometer and shortwave insolation observations by MIPS (Figs. 16a and 19c of K06) indicate that clouds are either directly above or shadowing the site at 1933, 1951, and 2000 UTC in agreement with the positions of water-saturated volumes based at 1.75–2 km near the MIPS location in the Lagrangian analysis (Fig. 15). Water-saturated volumes with bases of about 1.25 km are noted in the postfrontal rotor circulation (Figs. 15b–d). Successive frontal updraft plumes persist for up to 20 min as they traverse the frontal nose from its leading to its rear edge, and some of these plumes force small postfrontal water-saturated volumes. The intense deformation of the BL above the frontal nose occludes the dryline and lifts the former (surface-based) BL between the front and dryline to form a shallow ERL penetrated by cumulus based within the frontal rotor (Figs. 15e,f). The KA samples the folded transition layer above the ERL about 3.5 km west of the surface front as a horizontal temperature and moisture gradient resembling, though distinct from, the actual upper-level dryline to the east (Figs. 15e,f versus Fig. 10 of G06). Consistent with development of water-saturated volumes behind the surface front (Figs. 15e,f), the KA penetrates cumulus cloud tops between 1 and 3 km west of the surface front on its next (reverse direction) leg at  $\sim 2.2$  km AGL and 2009 UTC (not shown). Deeper front-to-rear flow north of the triple point is manifested as a shear zone including a closed, 20 km wide transient mesoscale circulation at 1 km in the postfrontal ERL around the triple point location (Fig. 3d,f,h).

Moist BL air is lifted into the ERL and its capping stable layer by updrafts, producing bulges of virtually cooler and more moist air than the adjacent quiescent inversion and forcing water saturated volumes where the local parcel LCL has been exceeded (Figs. 14–15). Conceptualizing the forcing of individual cumuli by observed longitudinal and transverse BL rolls (Fig. 16), a cloud is centered in a roll updraft above its level of nondivergence (e.g., as in Fig. 10 of Weckwerth et al. 1996). Although the roll updraft derives energy from buoyancy at heights below the updraft maximum, at higher (ERL) levels the (laterally entraining and mixed) updraft becomes negatively buoyant and penetrative. The special case of a homogeneous BL saturation point or LCL (Betts 1984), which results in a flat cloud base since all cloud-base parcels have the same LCL, may be produced locally by vertical advection in the mesoscale updraft when the roll is oriented with the

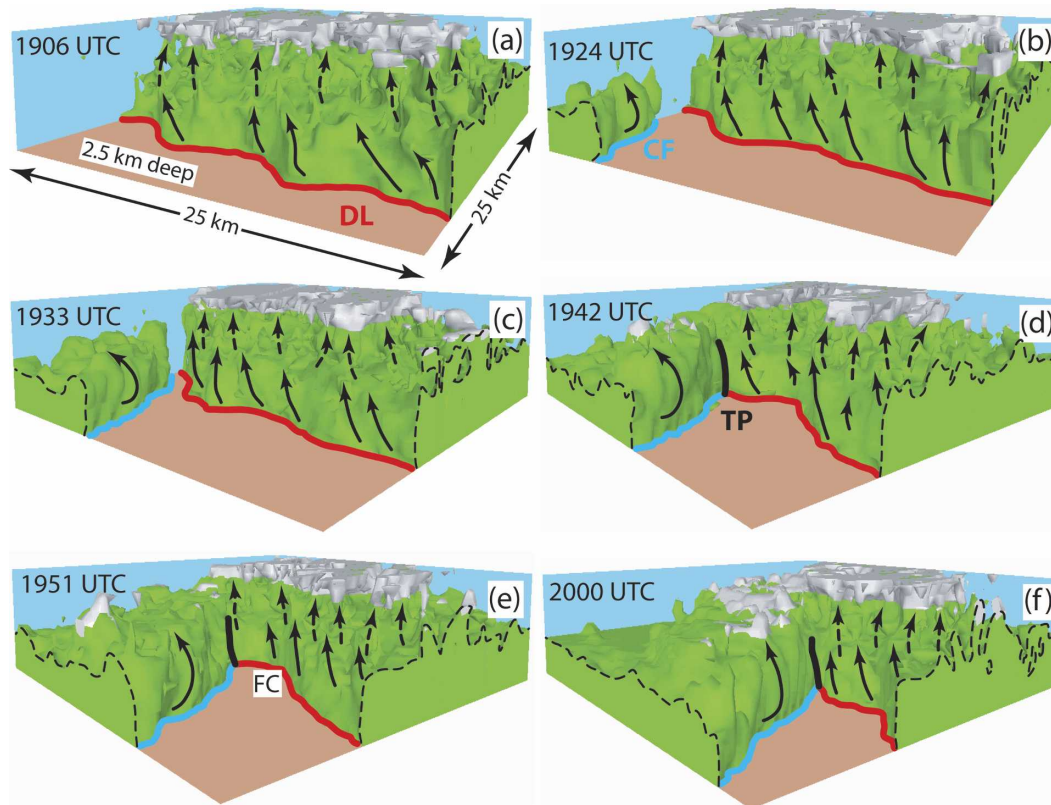


FIG. 13. Constant water vapor mixing ratio surface plots from Lagrangian analyses on 24 May 2002. Perspective views are oriented looking northeast; (a) 1906, (b) 1924, (c) 1933, (d) 1942, (e) 1951, (f) 2000 UTC. The  $8.7 \text{ g kg}^{-1}$  vapor mixing ratio surface is green, while water-saturated (i.e., 100% relative humidity) volumes are enclosed by white surfaces. Cumulus or cumulus fractus clouds are implied to exist within water-saturated volumes in the Lagrangian analyses. The positions of the surface cold front (CF) and dryline (DL) and the sloping 3D triple point (TP) curve are indicated by blue, red, and black solid curves, respectively. Dashed and solid black arrow-tipped curves denote selected moisture plumes in the ERL and moist BL, respectively, which in turn indicate the action of updrafts.

flow (Ziegler et al. 1997). Broadly speaking, the Lagrangian analysis results reveal an increasing LCL with height due to vertical mixing, which in turn produces slightly convex cloud-base surfaces due to parcels nearer individual cloud cores arriving from lower BL levels (Figs. 14–15).

Regarding surface layer variability due to roll effects in the BL (Weckwerth et al. 1996), it has been noted that the dry bands in the surface Lagrangian analysis west of the dryline are related to penetrative downdrafts of deep longitudinal rolls. Although the Lagrangian analysis assumes that the local grid-column sounding is correlated to surface measurements in BL updrafts, it makes no a priori assumption that observed longitudinal surface moisture bands are in phase with longitudinal rolls. For example, the surface moisture band just east of the dryline through the Fig. 14 cross section is connected to a prominently moist, cool longitudinal roll updraft at 1915 UTC (Fig. 10b versus Figs.

14c,d at  $x = 9 \text{ km}$ ). Other locations and times have less clearly defined connections between surface moisture bands and longitudinal rolls due to finite roll extent and advection of lifted air away from a downstream updraft edge (i.e., as microinsects and reflectivity in section 3a), periodic superposition of longitudinal and transverse roll modes locally creating more complex trajectories (e.g., Figs. 14c,d,k,l), and BL mixing of parcels from neighboring Lagrangian trajectories with differing source region properties (Ziegler et al. 2007). Although Weckwerth et al. (1996) suggested that the high-frequency surface layer variability (presumably forced by patch-scale surface layer sensible and latent heat fluxes) is unrelated to the overlying roll structure, it is speculated that roll-scale surface layer variability may be forced by downward roll-induced fluxes that overcompensate upward surface layer fluxes to provide a net flushing effect of the normally moist, unstable surface layer.

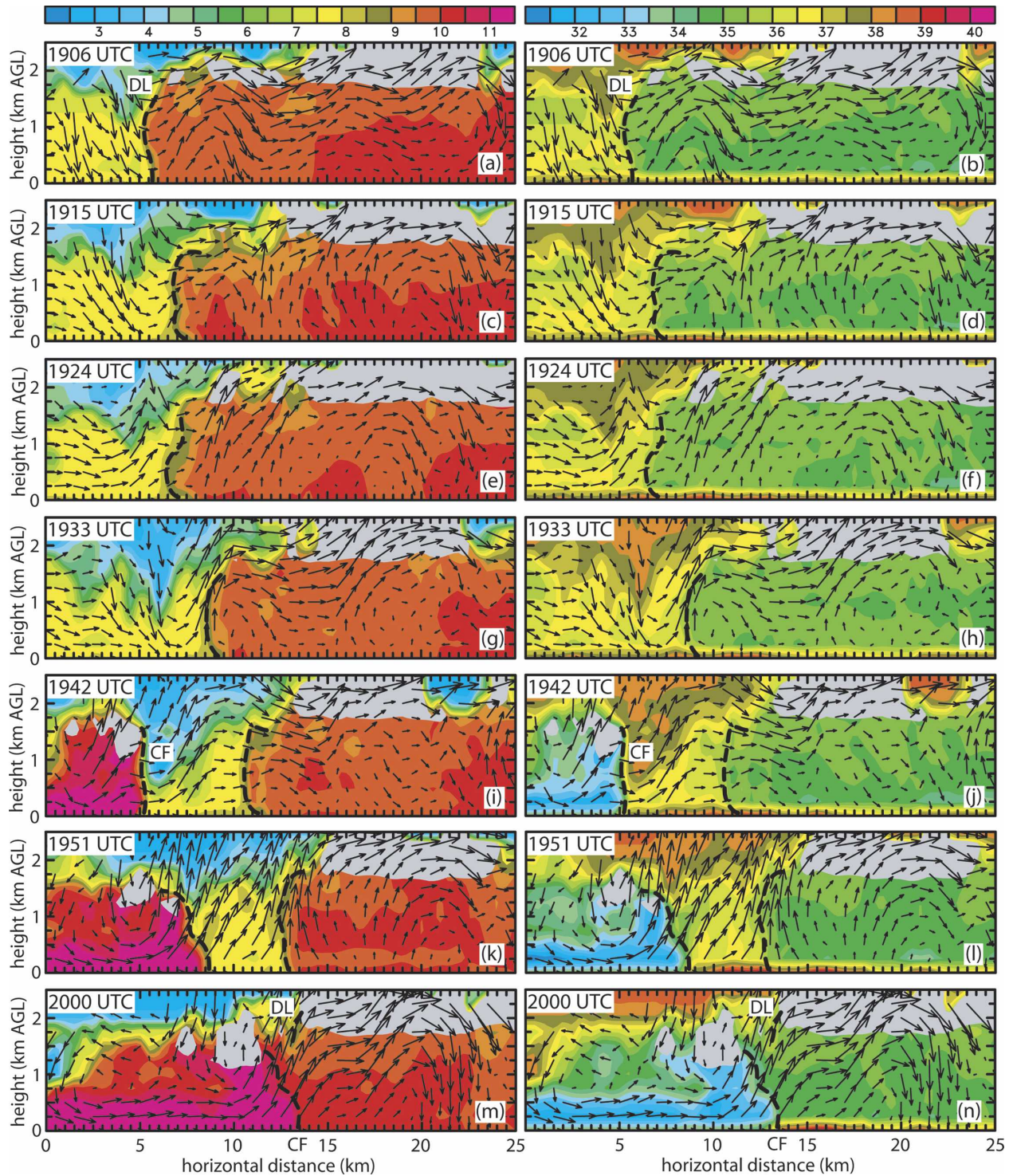


FIG. 14. Dryline-normal vertical cross sections of Lagrangian analyses near the KA stepped traverse pattern on 24 May 2002 (located in Fig. 10). (left) Vapor mixing ratio ( $\text{g kg}^{-1}$ ); (right) virtual potential temperature ( $^{\circ}\text{C}$ ); (top-to-bottom) 1906–1951 UTC. Gray-filled areas indicate water saturation (i.e., relative humidity  $>100\%$  or height  $Z > Z_{\text{LCL}}$ ). Every other velocity vector horizontally is plotted, with magnitude scaled by  $1 \text{ km} = 5 \text{ m s}^{-1}$ . Thick dashed curves locate leading edges of frontal and dryline moisture surfaces.

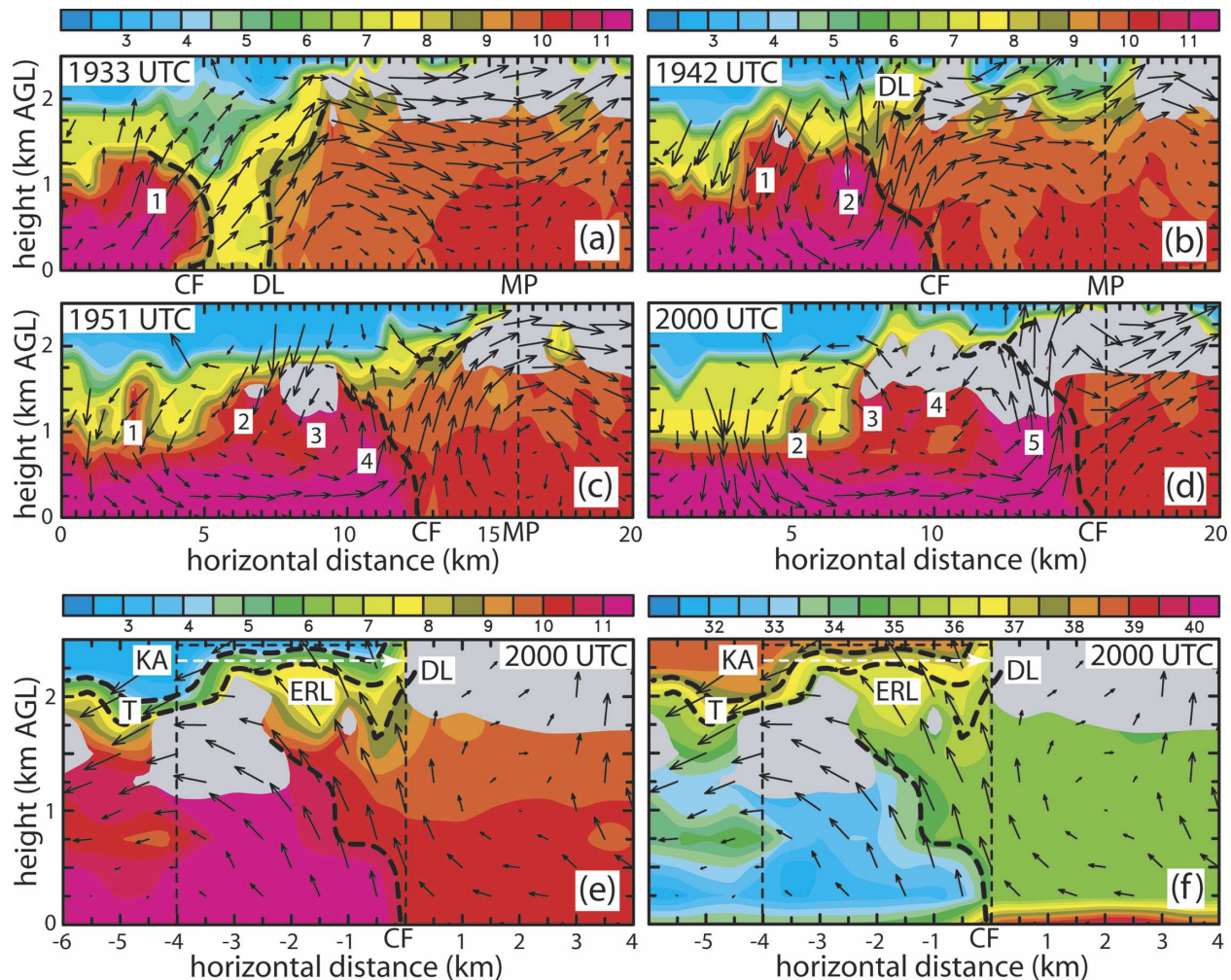


FIG. 15. High-resolution vertical cross sections through the cold front-dryline system from Lagrangian analysis output on 24 May 2002. Vapor mixing ratio ( $\text{g kg}^{-1}$ ) with ground-relative airflow in the northern cold frontal cross section (located in Figs. 10d–h) at (a) 1933, (b) 1942, (c) 1951, and (d) 2000 UTC. Southern cold frontal cross sections of (e) vapor mixing ratio ( $\text{g kg}^{-1}$ ) and (f) virtual potential temperature ( $^{\circ}\text{C}$ ) at 2000 UTC, with winds relative to the cold frontal motion from  $315^{\circ}$  at  $6.4 \text{ m s}^{-1}$  (located in Fig. 10h). In (e) and (f), the thin dashed box locates the WCR radar analysis domain of Fig. 10 in Geerts et al. (2006) while the dashed white arrow is the 1957:50–1959:50 UTC KA leg plotted in that figure. Gray-filled areas indicate water saturation (i.e., relative humidity  $>100\%$  or height  $Z > Z_{\text{LCL}}$ ). Every other velocity vector is plotted, with magnitude scaled by  $1 \text{ km} = 5 \text{ m s}^{-1}$ . Thick dashed curves locate leading edges of frontal and dryline moisture surfaces. Numbers denote successive postfrontal updraft and moisture plumes. A vertical dashed line labeled MP locates the plane-normal MIPS position about 2 km north of the cross section (e.g., Fig. 10). The symbols ERL and T refer to the elevated residual and capping transition layers overlying the ERL in the postfrontal 2006 M-GLASS sounding in Fig. 9a.

#### d. Comparison of water-saturated volumes in Lagrangian analysis and GOES-8 cumulus field

Although water-saturated volumes and observed clouds develop on either side of the surface cold front, the most extensive cloud and water-saturated areas are in the moist sector east of the dryline (Fig. 17). Series of updraft cores aligned in the direction of the subcloud airflow lift boundary layer moisture progressively higher following the parcel motion, forming cells and bands of high relative humidity (Figs. 17a,c,e,g). In

agreement with the relation of observed clouds to airflow (see section 4b), high relative humidity is generated in updraft cores and subsequently advected downstream in the Lagrangian analyses. Hence, both observed clouds and high relative humidity bands experience active and inactive periods in their evolution following the local parcel motion. The presence of southwest–northeast-oriented dryline-crossing convergence bands with enhanced moisture that support cumulus formation east of the dryline is in agreement with observations (Hane et al. 1997) and cloud–mesoscale

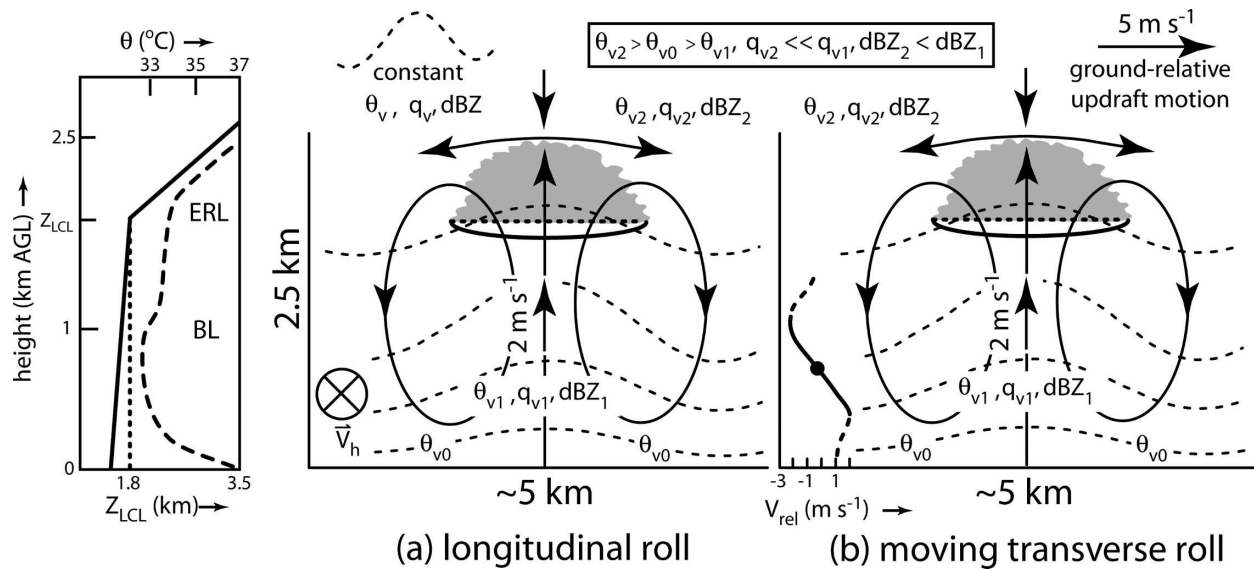


FIG. 16. Conceptual models of forced cumulus development by longitudinal and transverse horizontal convective rolls in the boundary layer on 24 May 2002. (a) Longitudinal roll with low-level horizontal wind directed into the plane; (b) transverse roll moving from left to right at  $5 \text{ m s}^{-1}$ , with inset showing the horizontal roll-normal, roll-relative wind component and associated inflection point (black dot) from the 1906 UTC M-CLASS sounding shown in Fig. 9c. The solid curves with arrowheads denote the boundary layer roll and the compensating clear air circulation forced by the penetrative roll updraft. Circulations in (a) and (b) are ground-relative and updraft-relative, respectively. In broad overall consistency with the radar wind analysis (e.g., Figs. 5 and 6), the rolls are approximated as circular in form with a maximum updraft of  $2 \text{ m s}^{-1}$  and a 2:1 aspect ratio (i.e., horizontal updraft spacing divided by depth). A gray-filled area illustrates a cumulus cloud. Left side: Conceptual profiles of LCL height (AGL) in a roll updraft, where the heavy solid line [i.e.,  $d(\text{LCL})/dz > 0$ ] corresponds to the solid (convex) cloud-base outline and the heavy dotted line [i.e.,  $d(\text{LCL})/dz = 0$ ] corresponds to the flat cloud base, and the reference potential temperature sounding (long dashed curve) east of the dryline (Ziegler et al. 2007). The roll updrafts are thermally buoyant in the lower BL below the maximum updraft and negatively buoyant (penetrative) in the ERL.

model simulations (Ziegler et al. 1997) of the severe 26 May 1991 Woodward, Oklahoma, dryline storm case.

The locations of clouds and water-saturated volumes are broadly consistent and are frequently located in or on the downwind edge of updraft cores (Figs. 17b,d,f,h). The coverage of clouds and water-saturated volumes becomes more extensive with time—particularly just ahead of and along the cold front—as the triple point moves southward. Some water-saturated volumes tend to form bands in the along-wind direction around the LCL height in locations where observed cloud tops may be nonbanded. As previously noted, the GOES-8 satellite would not resolve areas of cumulus fractus, and the latter would be characterized by very high mean relative humidity as cloud evaporates during mixing with drier overlying air. Furthermore, the absence of subgrid-scale mixing in the Lagrangian analysis may limit top-down entrainment drying of the very shallow downwind edges of water-saturated volumes to regions of elevated subsidence warming, possibly causing the total water-saturated volume to be overestimated. Retrieved postfrontal water-saturated volumes also appear to be somewhat overestimated relative to GOES-8 cloud tops at 2000 UTC

(Figs. 18g,h and 12), again possibly due to lack of sub-grid Lagrangian mixing in the analysis.

Weiss and Bluestein (2002) have suggested that the dryline and its associated secondary circulation are lifted at its triple-point intersection with an outflow boundary, possibly providing a focus for CI north of the triple point location. The outflow boundary in the Weiss and Bluestein (2002) case is normal to the dryline and their moist layer is much deeper than the outflow layer, implying that the solenoidal secondary outflow circulation is parallel to the dryline and thus would be able to advect the across-dryline thermal gradients to the north of the surface boundary. The deep frontal nose occludes the 24 May dryline from the surface to around 1.5 km (Figs. 13d,f, 14m,n, 15b–d, 17e–h), limiting front-to-rear horizontal advection of the dryline gradient in the present case to a relatively shallow layer within several hundred meters of cloud base.

*e. Evaluating the cumulus formation hypothesis in the IOR*

The parcel continuity principle for cumulus cloud formation requires that a rising air parcel must achieve its LCL while residing within the mesoscale updraft

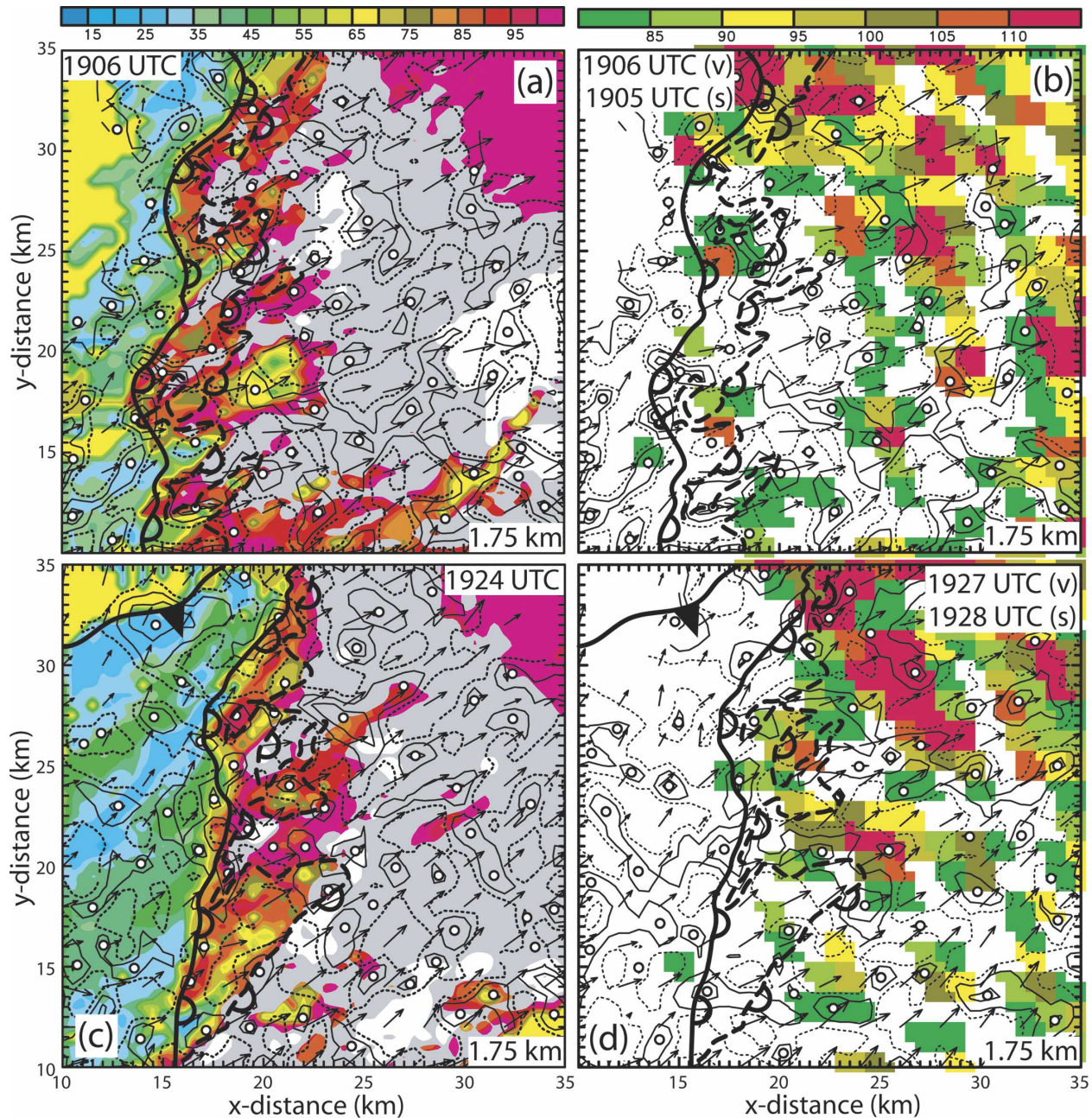


FIG. 17. Comparison of relative humidity and cloud analysis vs *GOES-8* cloud imagery at (a), (b) 1906, (c), (d) 1924, (e), (f) 1942, and (g), (h) 2000 UTC on 24 May 2002. (left) Retrieved relative humidity (%), horizontal winds, and vertical velocity at 1.75 km, with composited 2D satellite view of water saturation cores (i.e.,  $z/Z_{LCL} > 1.05$ ) at any level in each grid column (gray fill) and cloud depth greater than 0.3 km (white fill). (right) *GOES-8* visible image brightness  $> 80$  units (0–255 scale) with overlaid horizontal winds and vertical velocity at 1.75 km. Velocity vector magnitude is scaled by  $1 \text{ km} = 5 \text{ m s}^{-1}$ . Vertical velocity is contoured at a  $1 \text{ m s}^{-1}$  interval starting at  $1 \text{ m s}^{-1}$  (solid contour), while the dotted contour is zero vertical velocity. Black (white filled) circles locate updraft cores. Surface boundaries are located as in Fig. 10, while heavy dashed scalloped curve indicates the dryline at 1.75 km ( $q_v = 8.5 \text{ g kg}^{-1}$  contour).

that provides the lifting to water-saturate the parcel (ZR98). Following from the parcel continuity principle, it is hypothesized that the time required for an air parcel to cross and eventually exit the updraft horizontally

must equal or exceed the time required for the parcel to rise from its entrainment level  $H$  (i.e., the origin level of air entering the updraft) to its LCL. Obtaining time scales of horizontal and vertical advection from length

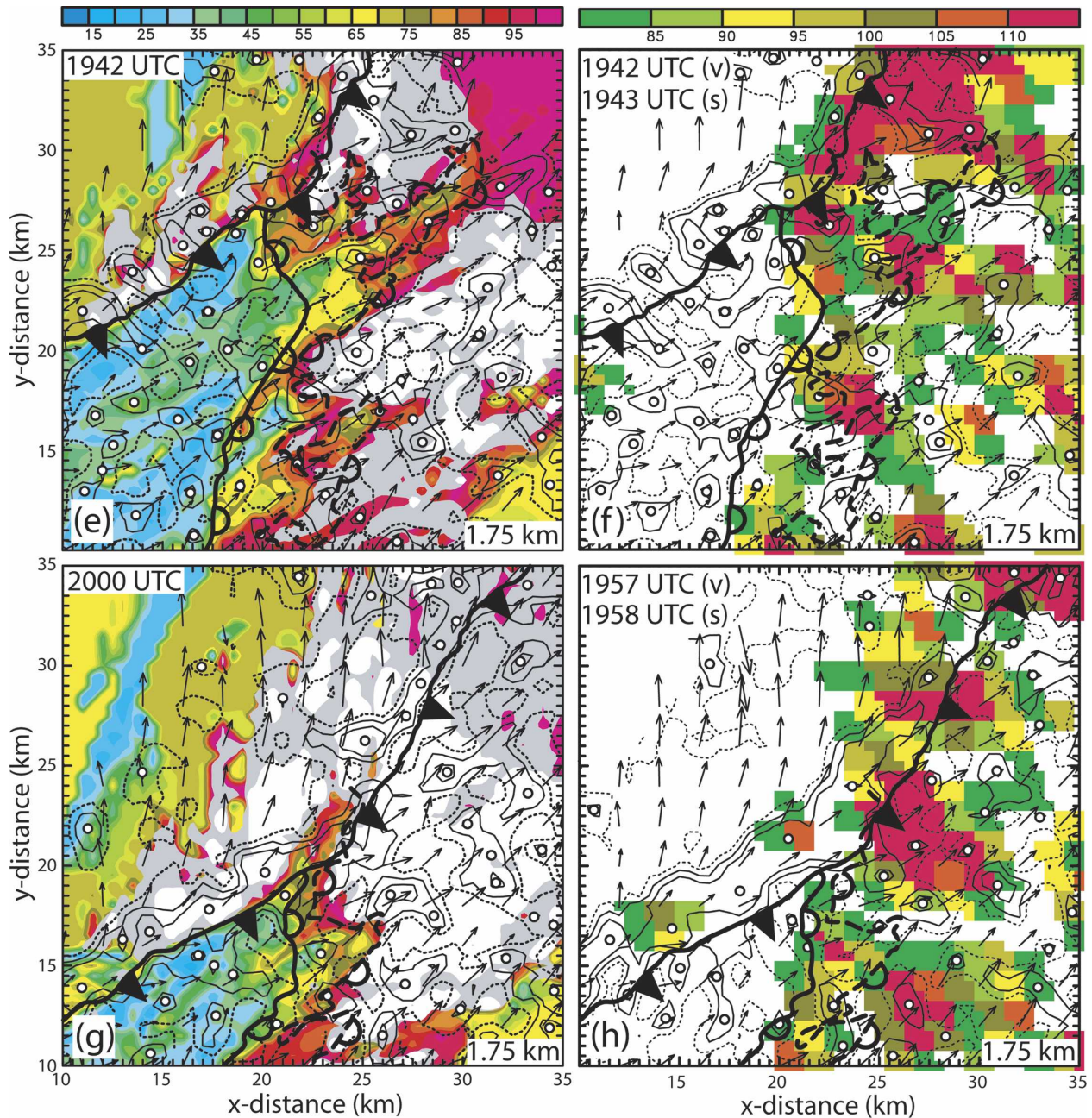


FIG. 17. (Continued)

divided by velocity scales, the latter time relation may be written as  $L/U \geq (LCL - H)/W$ , where  $L$  is the horizontal updraft length scale,  $U$  is the horizontal velocity scale, and  $W$  is the vertical velocity scale. Forming a dimensionless ratio  $R$  from the above time relationship yields  $R_{LCL} = WL/[U(LCL - H)] \geq 1$ . For a lifted parcel to achieve the LFC, it is hypothesized that  $R_{LFC} = WL/[U(LFC - H)] \geq 1$ .

The above scale parameters have been determined

from backward trajectories that originate from the bases of water-saturated volumes at 1.75 and 2 km to the east of the dryline in the 1924–2000 UTC Lagrangian analyses. The base of a water-saturated volume (i.e., equivalent to a cloud base) is indicated by the joint condition that  $Z^* = z/Z_{LCL} \geq 1$  at the current grid point and  $Z^* < 1$  at the next lower grid point. The duration of each trajectory corresponds to the smallest multiple of the Lagrangian analysis time spacing that

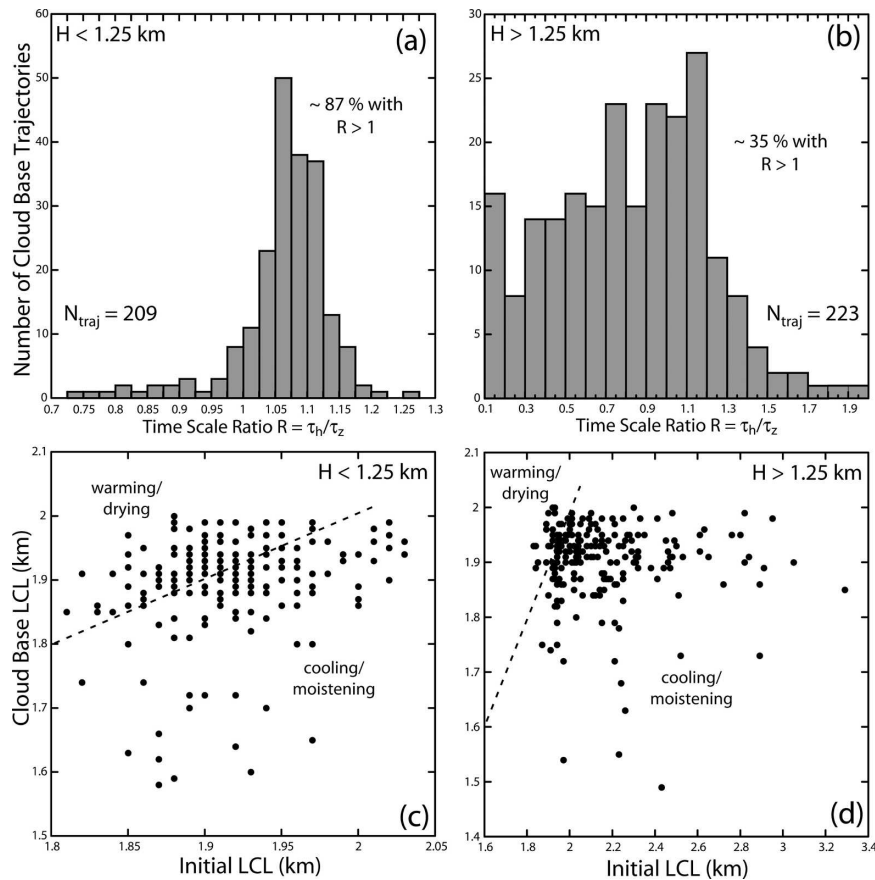


FIG. 18. Scaling parameters derived from upstream trajectories originating at bases of water-saturated volumes east of the dryline using output from the Lagrangian analyses on 24 May 2002. (a) Frequency distribution of entrainment level ( $H$ ) as a function of dimensionless time scale ratio  $R = \tau_H/\tau_z$  for  $H < 1.25$  km; (b) same as (a) but for  $H > 1.25$  km; (c) scatterplot of initial LCL value at beginning of forward trajectory (i.e., at the end of the backward trajectory) vs the cloud-base LCL value for  $H < 1.25$  km; (d) same as (c) but for  $H > 1.25$  km.

allows the trajectories to disperse throughout the BL (i.e., 18 min). The initial LCL value for a given trajectory is interpolated to the Lagrangian point from the earliest Lagrangian analysis time for that trajectory, while the length and velocity scales are time averages based on the displacement vector and time period between the initial and cloud-base locations.

About 87% of cloud-base trajectories originating in the moist BL below 1.25 km satisfy the dimensionless ratio  $R_{LCL} > 1$  (Fig. 18a; Table 3), verifying the cumulus formation hypothesis and identifying penetrative updraft plumes as the source of lifting of moist BL air to form clouds. The Lagrangian analysis mimics mixing on cumulus scales by objectively combining high-LCL trajectories based in the drier and warmer ERL with adjacent low-LCL, cloud-forming trajectories originating in the moist BL to maintain water saturation at cloud

edges. Hence, about 35% of cloud-forming trajectories originating in the ERL above 1.25 km satisfy the dimensionless ratio  $R_{LCL} > 1$  (Fig. 18b; Table 3), indicating the action of parcel moistening and cooling from mesoscale mixing prior to achieving cloud base. The initial LCL values tend to cluster around the corresponding cloud base LCL values for trajectories originating in the moist BL (Fig. 18c), with greater magnitude and frequency of decreased LCL for trajectories originating above 1.25 km (Fig. 18d), demonstrating that moist layer trajectories experience weaker mesoscale mixing than ERL trajectories. Other updraft trajectories which achieve high relative humidities without forming clouds either experience weaker vertical motion or entrain higher-LCL air than cloud-forming trajectories, then exit the updraft before water saturation is achieved (not shown).

TABLE 3. Values of length and velocity scales in different environments on 24 May 2002. Scales for the moist BL and ERL cases are mean values based on scatterplots of the various parameters of individual cloud-base trajectories (not shown). All values are to the nearest 0.1 units. In the CI case, the  $L$  and  $W$  scale values are picked, while the other scale values are estimated from dropsonde data (Fig. 19). The rightmost column lists either an  $R_{LCL}$  or  $R_{LFC}$  value, depending on whether the LCL or LFC value is substituted into the dimensionless ratio expression described in the text. The terms NA and Cu indicate not applicable and cumulus formation, respectively.

Environment	$U$ ( $\text{m s}^{-1}$ )	$L$ (km)	$H$ (km)	LCL (km)	LFC (km)	$W$ ( $\text{m s}^{-1}$ )	$R_{LCL}$ or $R_{LFC}$
IOR moist BL (Cu)	7	7	1	1.9	NA	1	7.0/6.3 $\sim$ 1
IOR ERL (Cu)	8	8	1.6	1.9	NA	0.4	3.2/2.4 $\sim$ 1
Western OK (CI area)	10	5	1	NA	1.6	1	5/6 $\sim$ 1

#### f. Evaluating the convection initiation hypothesis

Given a value of  $LFC = 3.1$  km (Figs. 9b,c), the condition  $R_{LFC} \sim 1$  would require a mean updraft strength substantially greater than  $1 \text{ m s}^{-1}$  to achieve CI in the IOR. Since the average updraft scale value in the ERL is only  $\sim 0.4 \text{ m s}^{-1}$  (Table 3) and would be expected to decrease with height in the overlying stable layer, deep convection is effectively suppressed near the triple point from a combination of stability, shear, and weak penetrative vertical motions or strong compensating downward motions (e.g., Figs. 14m,n, 15b–d).

What conditions support the initiation of deep convection in western Oklahoma, about 80 km east of the triple point? Subjective analysis based on parcel calculations of the west-to-east dropsonde array D1–D6 is used to infer the mesoscale environment on either side of the line of storms which developed between D2 and D3 (Fig. 2b). Dropsondes D1–D3 suggest that the moist BL east of the dryline is being undercut and lifted by a cooler, more moist, westward-moving internal BL<sup>4</sup> (Fig. 19). The moist internal BL is inferred to contact the surface between D2 and D3. A surge of southeasterly BL flow and enhanced cumulus cover along the leading edge of the implied convergence line (Fig. 2a versus Fig. 2b), coupled with the inferred west-to-east slope of the moist internal BL, support the inference of focused deep convergence and mesoscale updrafts at the CI location. The internal BL and convergence line are probably maintained by a horizontal flux directed toward the deeper, drier BL (Fig. 19) rather than by land surface characteristics and surface layer flux variations as described by Segal and Arritt (1992). W06 also inferred a mesoscale updraft at the CI location, although they based their conceptual interpretation on the coincidence of a dropsonde-deduced upward moisture bulge and a lidar-detected aerosol plume.

Horizontally variable inhibiting layers of parcel virtual temperature deficit are present above both the

moist BL and the ERL in the present analysis (Fig. 19). At the CI location, the BL lid achieves a local minimum while the ERL lid does not exist. A strong lapse rate, a recognized principle ingredient for deep convection (Doswell 1987) that would assist rapid intensification of cloudy updrafts exceeding the LFC, is present above the LFC around the CI location (not shown). Assuming scale parameter values based on the dropsonde observations at the CI location (Table 3), an updraft strength of  $1 \text{ m s}^{-1}$  would be sufficient to attain a value of  $R_{LFC} \sim 1$ . Thus, it is speculated that the collocation of a locally weak lid with enhanced moisture and deep mesoscale lifting along a sloping internal BL between D2 and D3 provide the ingredients for CI in the region east of the triple point and IOR on 24 May 2002. A very similar roll-induced CI event east of a dryline may have initiated the development of the tornadic Moore, Oklahoma supercell on 3 May 1999 (Edwards et al. 2000).

## 5. Conclusions

This paper reports a study of cumulus formation and convection initiation near a cold frontal-dryline triple point intersection using mobile surface and airborne BL observations on 24 May 2002 during the International H<sub>2</sub>O Project (IHOP). A high-resolution analysis of up to four mobile ground-based radars defines the evolving kinematic and reflectivity structure of the boundary layer. Analyses of in situ data from mobile mesonets, aircraft, and sounding systems define the finescale gradients and evolution of moisture and virtual potential temperature delineating the cold front, the dryline, and the neighboring BL. The assimilation of all in situ measurements using the 4D wind fields and a new Lagrangian analysis scheme provides output fields of vapor mixing ratio, virtual potential temperature, and LCL height on a subdomain of the radar analysis grid. Boundary layer evolution and Lagrangian water-saturated volume formation are placed in the context of gridded analyses of GOES-8 visible imagery and single-camera photogrammetric cloud-base coverage.

The radar and Lagrangian analyses reveal the pres-

<sup>4</sup> An internal boundary layer is a shallow BL that displaces a deeper BL (Pielke 1984, p. 166).

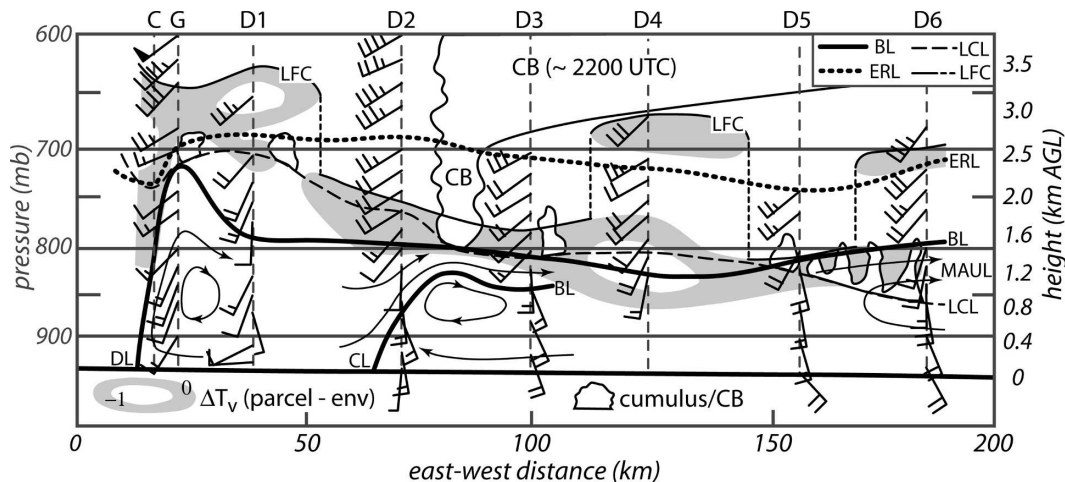


FIG. 19. Subjective analysis of Learjet dropsondes and mobile ground-based soundings east of the dryline on 24 May 2002 in a west–east plane containing the dropsondes. The dropsondes D1–D6 reached the surface in the period 2041–2056 UTC, C = 1906 UTC M-CLASS, and G = 1920 UTC M-GLASS. The location of the dropsondes is indicated in Fig. 2a, while the locations of the convective line and anvil at 2200 UTC relative to the dropsondes are indicated in Fig. 2b. Sounding indices are derived from parcel theory assuming the lowest 50-mb averaged parcel. A heavy black curve denotes the top of the moist BL, while the heavy dotted line locates an ERL. The thin-dashed and solid-dashed curves locate the LCL and the LFC of the main CAPE-bearing layer in the sounding, respectively. A moist absolutely unstable layer or MAUL (Kain and Fritsch 1998) with buoyancy  $\sim 10 \text{ J kg}^{-1}$  is present near the eastern end of the domain. Streamlines conceptually depict the circulations at the dryline, the inferred convergence line, and the MAUL, the latter circulations inferred from 1D, mesoscale convergence of the dropsonde winds. A half wind barb is  $2.5 \text{ m s}^{-1}$ , a full barb is  $5 \text{ m s}^{-1}$ , and a filled barb is  $25 \text{ m s}^{-1}$ . Gray shading denotes a virtual temperature deficit  $\Delta T_v$  of a lifted BL parcel with respect to its environment of up to  $-1^\circ\text{C}$ , while interior unshaded areas denote  $\Delta T_v < -1^\circ\text{C}$ .

ence of longitudinal and transverse BL roll circulations, including an intense rotor circulation behind the leading edge of the cold front and localized updrafts and secondary vertical circulations along the dryline. The transverse rolls, which appear to be caused by an inflection point instability, tilt ambient roll-parallel shear to produce transverse bands of positive and negative vorticity aligned with the upwind and downwind roll updraft flanks respectively. A remarkable finding of the time-spaced wind analyses is the apparent persistence of individual updraft, vertical vorticity, and reflectivity cores and transverse rolls for periods of up to 30 min or more while moving approximately with the local mean BL wind. Persistent longitudinal rolls are also noted on either side of the dryline.

Satellite cloud images and single-camera ground photogrammetry imply that clouds tend to develop either over or on the downwind edge of BL updrafts, with a tendency for clouds to elongate and dissipate in the downwind direction relative to cloud layer winds due to weakening updrafts and mixing with drier overlying air. Cloud base areas are 25%–50% of cloud-top areas, and bases of all cumuli are above the level of nondivergence in the updraft plumes that force cloud formation, leading to the speculation that individual clouds act as detrain plumes.

The Lagrangian and radar analyses support the parcel continuity principle for cumulus formation, which requires that rising moist air parcels achieve their LCL before exiting the updraft following the updraft-relative horizontal flow (ZR98). Moisture is lifted in plumes from the top of the moist BL to cloud bases east of the dryline via penetrative dry convective updrafts in the overlying ERL. Despite locally small values of lid strength, absence of CI near the triple point is likely a result of weak, nonpenetrative updrafts in the CIN-bearing layer overlying the cumulus-filled ERL. An analysis of moisture, winds, and parcel stability indices based on a dropsonde profile east of the dryline suggests the collocation of an internal moist BL, a localized deep mesoscale updraft and roll circulation, and reduced CIN in the overlying stable layer. Application of the parcel continuity principle implies that local BL updrafts of only  $\sim 1 \text{ m s}^{-1}$  would be capable of achieving the observed CI event given observed shear and stratification about 80 km east of the triple point.

*Acknowledgments.* We thank the numerous participants, whose collective efforts made IHOP a success, including the groups who operated the ground-based mobile facilities and aircraft and Tammy Weckwerth and David Parsons (NCAR) who led IHOP. We grate-

fully acknowledge the assistance of David Stensrud (NSSL), who performed the inflection point instability analysis using the Stensrud-Shirer model, and the efforts of two anonymous reviewers whose comments helped to improve the manuscript. Dennis Neelson, Sherman Fredrickson, and Doug Kennedy (NSSL) expertly fabricated and maintained the NSSL mobile ground-based facilities, including the redesign and construction of new, second-generation mobile mesonets. Funding for deploying NSSL's IHOP mobile facilities and for data analysis was provided under NSF Grant ATM-0130316. Other funding to fabricate and deploy NSSL's IHOP mobile facilities and to analyze IHOP data was granted by the High Performance Computing Consortium (HPCC), the United States Weather Research Program (USWRP), and the National Severe Storms Laboratory Director's Discretionary Fund (all NOAA agencies). Funding for DOW radar deployment and data analysis was provided under NSF Grant ATM-0208651.

## REFERENCES

- Arnott, N. R., Y. P. Richardson, J. M. Wurman, and E. N. Rasmussen, 2006: Relationship between a weakening cold front, mesocyclones, and cloud development on 10 June 2002 during IHOP. *Mon. Wea. Rev.*, **134**, 311–335.
- Atkins, N. T., R. M. Wakimoto, and T. M. Weckwerth, 1995: Observations of the sea-breeze front during CAPE. Part II: Dual-Doppler and aircraft analysis. *Mon. Wea. Rev.*, **123**, 944–969.
- , —, and C. L. Ziegler, 1998: Observations of the finescale structure of a dryline during VORTEX 95. *Mon. Wea. Rev.*, **126**, 525–550.
- Banacos, P. C., and D. M. Schultz, 2005: The use of moisture flux convergence in forecasting convective initiation: Historical and operational perspectives. *Wea. Forecasting*, **20**, 351–366.
- Barnes, S. L., 1973: Mesoscale objective map analysis using weighted time-series observations. NOAA Tech. Memo. ERL NSSL-62, 60 pp.
- Betts, A. K., 1984: Boundary layer thermodynamics of a High Plains severe storm. *Mon. Wea. Rev.*, **112**, 2199–2211.
- Biggerstaff, M., and Coauthors, 2005: The Shared Mobile Atmospheric Research and Teaching (SMART) radar: A collaboration to enhance research and teaching. *Bull. Amer. Meteor. Soc.*, **86**, 1263–1274.
- Bluestein, H. B., E. W. McCaul Jr., G. P. Byrd, and G. R. Woodall, 1988: Mobile sounding observations of a tornadic storm near the dryline: The Canadian, Texas storm of 7 May 1986. *Mon. Wea. Rev.*, **116**, 1790–1804.
- Brooks, H. E., C. A. Doswell III, and R. A. Maddox, 1992: On the use of mesoscale and cloud-scale models in operational forecasting. *Wea. Forecasting*, **7**, 120–132.
- Brown, R. A., 1980: Longitudinal instabilities and secondary flows in the planetary boundary layer: A review. *Rev. Geophys. Space Phys.*, **18**, 683–697.
- Craven, J. P., R. E. Jewell, and H. E. Brooks, 2002: Comparison between observed convective cloud-base heights and lifting condensation level for two different lifted parcels. *Wea. Forecasting*, **17**, 885–890.
- Davies-Jones, R. P., 1974: Discussion of measurements inside high-speed thunderstorm updrafts. *J. Appl. Meteor.*, **13**, 710–717.
- Doswell, C. A., III, 1987: The distinction between large-scale and mesoscale contribution to severe convection: A case study example. *Wea. Forecasting*, **2**, 3–16.
- , H. E. Brooks, and R. A. Maddox, 1996: Flash flood forecasting: An ingredients-based methodology. *Wea. Forecasting*, **11**, 560–581.
- Edwards, R., R. L. Thompson, and J. G. LaDue, 2000: Initiation of Storm A (3 May 1999) along a possible horizontal convective roll. Preprints, *20th Conf. on Severe Local Storms*, Orlando, FL, Amer. Meteor. Soc., 60–63.
- Fritsch, J. M., and Coauthors, 1998: Quantitative precipitation forecasting: Report of the Eighth Prospectus Development Team, U.S. Weather Research Program. *Bull. Amer. Meteor. Soc.*, **79**, 285–299.
- Geerts, B., and Q. Miao, 2005: The use of millimeter Doppler radar echoes to estimate vertical air velocities in the fair-weather convective boundary layer. *J. Atmos. Oceanic Technol.*, **22**, 225–246.
- , R. Damiani, and S. Haimov, 2006: Fine-scale vertical structure of a cold front as revealed by an airborne Doppler radar. *Mon. Wea. Rev.*, **134**, 251–272.
- Gossard, E. E., and W. R. Moninger, 1975: The influence of a capping inversion on the dynamic and convective instability of a boundary layer model with shear. *J. Atmos. Sci.*, **32**, 2111–2124.
- Hane, C. E., H. B. Bluestein, T. M. Crawford, M. E. Baldwin, and R. M. Rabin, 1997: Severe thunderstorm development in relation to along-dryline variability: A case study. *Mon. Wea. Rev.*, **125**, 231–251.
- , R. M. Rabin, T. M. Crawford, H. B. Bluestein, and M. E. Baldwin, 2002: A case study of severe storm development along a dryline within a synoptically active environment. Part II: Multiple boundaries and convective initiation. *Mon. Wea. Rev.*, **130**, 900–920.
- Johns, R. H., and C. A. Doswell III, 1992: Severe local storms forecasting. *Wea. Forecasting*, **7**, 588–612.
- Kain, J. S., and J. M. Fritsch, 1998: Multiscale convective overturning in mesoscale convective systems: Reconciling observations, simulations, and theory. *Mon. Wea. Rev.*, **126**, 2254–2273.
- Kanak, K. M., D. K. Lilly, and J. T. Snow, 2000: The formation of vertical vortices in the convective boundary layer. *Quart. J. Roy. Meteor. Soc.*, **126**, 2789–2810.
- Karan, H., and K. Knupp, 2006: Mobile Integrated Profiler System (MIPS) observations of low-level convergent boundaries during IHOP. *Mon. Wea. Rev.*, **134**, 92–112.
- Koch, S. E., and W. L. Clark, 1999: A nonclassical cold front observed during COPS-91: Frontal structure and the process of severe storm initiation. *J. Atmos. Sci.*, **56**, 2862–2890.
- , M. DesJardins, and P. J. Kocin, 1983: An interactive Barnes objective map analysis scheme for use with satellite and conventional data. *J. Climate Appl. Meteor.*, **22**, 1487–1503.
- Lilly, D. K., 1966: On the instability of Ekman boundary flow. *J. Atmos. Sci.*, **23**, 481–494.
- Markowski, P. M., C. Hannon, and E. Rasmussen, 2006: Observations of convection initiation “failure” from the 12 June 2002 IHOP deployment. *Mon. Wea. Rev.*, **134**, 375–405.
- McCarthy, J., and S. E. Koch, 1982: The evolution of an Oklaho-

- ma dryline. Part I: A meso- and subsynoptic-scale analysis. *J. Atmos. Sci.*, **39**, 225–236.
- Miller, L. J., M. A. LeMone, W. Blumen, R. L. Grossman, N. Gamage, and R. J. Zamora, 1996: The low-level structure and evolution of a dry arctic cold front over the central United States. Part I: Mesoscale observations. *Mon. Wea. Rev.*, **124**, 1648–1675.
- Mohr, C. G., L. J. Miller, R. L. Vaughan, and H. W. Frank, 1986: The merger of mesoscale datasets into a common Cartesian format for efficient and systematic analyses. *J. Atmos. Oceanic Technol.*, **3**, 144–161.
- Murphey, H. V., R. M. Wakimoto, C. Flamant, and D. E. Kingsmill, 2006: Dryline on 19 June 2002 during IHOP. Part I: Airborne Doppler and LEANDRE II analyses of the thin line structure and convection initiation. *Mon. Wea. Rev.*, **134**, 406–430.
- Oye, R., C. Mueller, and S. Smith, 1995: Software for radar translation, visualization, editing, and interpolation. Preprints, *27th Conf. on Radar Meteorology*, Vail, CO, Amer. Meteor. Soc., 359–361.
- Parker, L., R. M. Welch, and D. J. Musil, 1986: Analysis of spatial inhomogeneities in cumulus clouds using high spatial resolution Landsat data. *J. Appl. Meteor.*, **25**, 1301–1314.
- Pielke, R. A., Sr., 1984: *Mesoscale Meteorological Modeling*. Academic Press, 612 pp.
- Rasmussen, E. N., R. Davies-Jones, and R. L. Holle, 2003: Terrestrial photogrammetry of weather images acquired in uncontrolled circumstances. *J. Atmos. Oceanic Technol.*, **20**, 1790–1803.
- Rockwood, A. A., and R. A. Maddox, 1988: Mesoscale and synoptic scale interactions leading to intense convection: The case of 7 June 1982. *Wea. Forecasting*, **3**, 51–68.
- Rust, W. D., D. W. Burgess, R. A. Maddox, L. C. Showell, T. C. Marshall, and D. K. Lauritsen, 1990: Testing a mobile version of a cross-chain Loran atmospheric (M-CLASS) sounding system. *Bull. Amer. Meteor. Soc.*, **71**, 173–180.
- Schultz, D. M., 2005: A review of cold fronts with prefrontal troughs and wind shifts. *Mon. Wea. Rev.*, **133**, 2449–2472.
- Segal, M., and R. W. Arritt, 1992: Nonclassical mesoscale circulations caused by surface sensible heat-flux gradients. *Bull. Amer. Meteor. Soc.*, **73**, 1593–1604.
- Shapiro, M. A., T. Hampel, D. Rotzoll, and F. Mosher, 1985: The frontal hydraulic head: A micro- $\alpha$  scale ( $\sim 1$  km) triggering mechanism for mesoconvective weather systems. *Mon. Wea. Rev.*, **113**, 1166–1183.
- Stensrud, D. J., and H. N. Shirer, 1988: Development of boundary layer rolls from dynamic instabilities. *J. Atmos. Sci.*, **45**, 1007–1019.
- , and J.-W. Bao, 1992: Behaviors of variational and nudging assimilation techniques with a chaotic low-order model. *Mon. Wea. Rev.*, **120**, 3016–3028.
- Straka, J. M., E. N. Rasmussen, and S. E. Fredrickson, 1996: A mobile mesonet for fine scale meteorological observations. *J. Atmos. Oceanic Technol.*, **13**, 921–936.
- Stull, R. B., 1985: A fair-weather cumulus cloud classification scheme for mixed-layer studies. *J. Climate Appl. Meteor.*, **24**, 49–56.
- Wakimoto, R. M., H. V. Murphey, E. V. Browell, and S. Ismail, 2006: The “triple point” on 24 May 2002 during IHOP. Part I: Airborne Doppler and LASE analyses of the frontal boundaries and convection initiation. *Mon. Wea. Rev.*, **134**, 231–250.
- Weckwerth, T. M., and D. B. Parsons, 2006: A review of convection initiation and motivation for IHOP\_2002. *Mon. Wea. Rev.*, **134**, 5–22.
- , J. W. Wilson, and R. M. Wakimoto, 1996: Thermodynamic variability within the convective boundary layer due to horizontal convective rolls. *Mon. Wea. Rev.*, **124**, 769–784.
- , and Coauthors, 2004: An overview of the International H<sub>2</sub>O Project (IHOP\_2002) and some preliminary highlights. *Bull. Amer. Meteor. Soc.*, **85**, 253–277.
- Weiss, C. C., and H. B. Bluestein, 2002: Airborne pseudo-dual Doppler analysis of a dryline–outflow boundary intersection. *Mon. Wea. Rev.*, **130**, 1207–1226.
- , —, and A. L. Pazmany, 2006: Finescale radar observations of the 22 May 2002 dryline during the International H<sub>2</sub>O Project (IHOP). *Mon. Wea. Rev.*, **134**, 273–293.
- Wilson, J. W., and W. E. Schreiber, 1986: Initiation of convective storms at radar-observed boundary-layer convergence lines. *Mon. Wea. Rev.*, **114**, 2516–2536.
- , G. B. Foote, N. A. Crook, J. C. Fankhauser, C. G. Wade, J. D. Tuttle, C. K. Mueller, and S. K. Krueger, 1992: The role of boundary-layer convergence zones and horizontal rolls in the initiation of thunderstorms: A case study. *Mon. Wea. Rev.*, **120**, 1785–1815.
- Wurman, J., 2001: The DOW mobile multiple Doppler network. Preprints, *30th Int. Conf. on Radar Meteorology*, Munich, Germany, Amer. Meteor. Soc., 95–97.
- , J. Straka, E. Rasmussen, M. Randall, and A. Zahrai, 1997: Design and deployment of a portable, pencil-beam, pulsed, 3-cm Doppler radar. *J. Atmos. Oceanic Technol.*, **14**, 1502–1512.
- Ziegler, C. L., and C. E. Hane, 1993: An observational study of the dryline. *Mon. Wea. Rev.*, **121**, 1134–1151.
- , and E. N. Rasmussen, 1998: The initiation of moist convection at the dryline: Forecasting issues from a case study perspective. *Wea. Forecasting*, **13**, 1106–1131.
- , W. J. Martin, R. A. Pielke, and R. L. Walko, 1995: A modeling study of the dryline. *J. Atmos. Sci.*, **52**, 263–285.
- , T. J. Lee, and R. A. Pielke Sr., 1997: Convective initiation at the dryline: A modeling study. *Mon. Wea. Rev.*, **125**, 1001–1026.
- , D. Kennedy, and E. N. Rasmussen, 2004: A wireless network for collection and synthesis of mobile mesoscale weather observations. *J. Atmos. Oceanic Technol.*, **21**, 1659–1669.
- , M. S. Buban, and E. N. Rasmussen, 2007: A Lagrangian objective analysis technique for assimilating in situ observations with multiple radar-derived airflow. *Mon. Wea. Rev.*, **135**, 2417–2442.